UAV-Multispectral Sensed Data Band Co-Registration Framework

Jocival Dantas Dias Junior

Universidade Federal de Uberlândia
Faculdade de Computação
Programa de Pós-Graduação em Ciência da Computação

Uberlândia

2020

Jocival Dantas Dias Junior

UAV-Multispectral Sensed Data Band Co-Registration Framework

Dissertação de mestrado apresentada ao Programa de Pós-graduação da Faculdade de Computação da Universidade Federal de Uberlândia como parte dos requisitos para a obtenção do título de Mestre em Ciência da Computação.

Área de concentração: Ciência da Computação

Orientador: Prof. Dr. André Ricardo Backes
Coorientador: Prof. Dr. Maurício Cunha Escarpinati

Uberlândia

2020

UNIVERSIDADE FEDERAL DE UBERLÂNDIA

Coordenação do Programa de Pós-Graduação em Ciência da Computação

Av. João Naves de Ávila, nº 2121, Bloco 1A, Sala 243 - Bairro Santa Mônica, Uberlândia-MG, CEP 38400-902

Telefone: (34) 3239-4470 - www.ppgco.facom.ufu.br - cpgfacom@ufu.br

ATA DE DEFESA - PÓS-GRADUAÇÃO

Programa de Pós-Graduação em:	Ciência da Computação				
Defesa de:	Dissertação de Mestrado Acadêmico, 05/2020, PPGCO				
Data:	17 de fevereiro de 2020	Hora de início:	**09hrs10min**	Hora de encerramento:	**11hrs30min**
Matrícula do Discente:	11812CCP019				
Nome do Discente:	Jocival Dantas Dias Júnior				
Título do Trabalho:	UAV-Multispectral Sensed Data Band Co-Registration Framework				
Área de concentração:	Ciência da Computação				
Linha de pesquisa:	Ciência de Dados				
Projeto de Pesquisa de vinculação:	-				

Reuniu-se na sala 1B132, Bloco 1B, Campus Santa Mônica, da Universidade Federal de Uberlândia, a Banca Examinadora, designada pelo Colegiado do Programa de Pós-graduação em Ciência da Computação, assim composta: Professores Doutores: Jefferson Rodrigo de Souza- FACOM/UFU, Maurício Marengoni - MACKENZIE, Maurício Cunha Escarpinati - FACOM/UFU (coorientador) e André Ricardo Backes - FACOM/UFU, orientador do candidato.

Ressalta-se que o Prof. Dr. Maurício Marengoni participou da defesa por meio de videoconferência desde a cidade de São Paulo -SP. Os outros membros da banca e o aluno participaram in loco.

Iniciando os trabalhos o presidente da mesa, Prof. Dr. André Ricardo Backes, apresentou a Comissão Examinadora e o candidato, agradeceu a presença do público, e concedeu ao Discente a palavra para a exposição do seu trabalho. A duração da apresentação do Discente e o tempo de arguição e resposta foram conforme as normas do Programa.

A seguir o senhor presidente concedeu a palavra, pela ordem sucessivamente, aos examinadores, que passaram a arguir o candidato. Ultimada a arguição, que se desenvolveu dentro dos termos regimentais, a Banca, em sessão secreta, atribuiu o resultado final, considerando o candidato:

Aprovado

Esta defesa faz parte dos requisitos necessários à obtenção do título de Mestre.

O competente diploma será expedido após cumprimento dos demais requisitos,

conforme as normas do Programa, a legislação pertinente e a regulamentação interna da UFU.

Nada mais havendo a tratar foram encerrados os trabalhos. Foi lavrada a presente ata que após lida e achada conforme foi assinada pela Banca Examinadora.

Documento assinado eletronicamente por **Jefferson Rodrigo de Souza**, **Professor(a) do Magistério Superior**, em 17/02/2020, às 15:29, conforme horário oficial de Brasília, com fundamento no art. 6º, § 1º, do Decreto nº 8.539, de 8 de outubro de 2015.

Documento assinado eletronicamente por **André Ricardo Backes**, **Professor(a) do Magistério Superior**, em 17/02/2020, às 16:22, conforme horário oficial de Brasília, com fundamento no art. 6º, § 1º, do Decreto nº 8.539, de 8 de outubro de 2015.

Documento assinado eletronicamente por **Maurício Marengoni**, **Usuário Externo**, em 18/02/2020, às 09:27, conforme horário oficial de Brasília, com fundamento no art. 6º, § 1º, do Decreto nº 8.539, de 8 de outubro de 2015.

Documento assinado eletronicamente por **Mauricio Cunha Escarpinati**, **Professor(a) do Magistério Superior**, em 27/02/2020, às 11:47, conforme horário oficial de Brasília, com fundamento no art. 6º, § 1º, do Decreto nº 8.539, de 8 de outubro de 2015.

A autenticidade deste documento pode ser conferida no site https://www.sei.ufu.br/sei/controlador_externo.php?acao=documento_conferir&id_orgao_acesso_externo=0, informando o código verificador **1871170** e o código CRC **51A73C20**.

Referência: Processo nº 23117.007481/2020-24   SEI nº 1871170

Dedico este trabalho a todos que sempre me ampararam, em especial aos meus pais Sandra Divina de Jesus Urzeda e Jocival Dantas Dias, meus avós Joseva, Sinval (in memoriam), Iracema (in memoriam) e Jose Balduíno (in memoriam), aos meus irmãos John e Lenne e ao meu amor Caroline.

Agradecimentos

À Deus, por ter me dado o privilégio da vida e a oportunidade de trilhar o caminho que me levou a conclusão de mais uma etapa.

Aos meus pais pela sabedoria, ensinamentos e educação que me levaram a ser a pessoa que sou hoje, aos meus irmãos que sempre se dedicaram em me apoiar e orientar em todos os momentos e a minha namorada, Caroline A. Marçal, por todo o amor, carinho, amizade e companheirismo nesses dois anos.

Ao meu orientador Prof. Dr. Andre Ricardo Backes e coorientador Prof. Dr. Maurício Cunha Escarpinati pela orientação, amizade, críticas, ensinamentos e oportunidades que me foram dadas.

Aos Profs. Drs. Bruno Augusto Nassif Travençolo, Daniel Duarte Abdala, Fabiano Azevedo Dorça e Ronaldo de Castro Oliveira por terem contribuído para minha formação profissional e pessoal.

Aos Profs. da Faculdade de Computação que tive a oportunidade de ser discente. E a todos os técnicos que sempre estiveram a disposição para me atender.

Resumo

A agricultura de precisão se beneficiou muito das novas tecnologias ao longo dos anos. O uso de sensores multiespectrais e hiperespectrais acoplados aos Veículos Aéreos Não Tripulados (VANT) permitiu que as fazendas monitorassem as lavouras, melhorassem o uso de recursos e reduzissem os custos. Apesar de amplamente utilizadas, as imagens multiespectrais apresentam um desalinhamento natural entre os vários espectros devido ao uso de diferentes sensores. A variação do espectro analisado também leva à perda de características entre as bandas, o que dificulta o processo de detecção de atributos entre as bandas, o que torna complexo o processo de alinhamento. Neste trabalho, propomos um novo *framework* para o processo de alinhamento entre as bandas com base em duas premissas: i) o desalinhamento natural é um atributo da câmera, e por esse motivo ele não é alterado durante o processo de aquisição; ii) a velocidade de deslocamento do VANT, quando comparada à velocidade entre a aquisição da primeira e a última banda, não é suficiente para criar distorções significativas. Os resultados obtidos foram comparados com o padrão ouro gerado por um especialista e com outros métodos presentes na literatura. O *framework* proposto teve um *back-projection error* (BP) de $0,425$ pixels, sendo este resultado 335% melhor aos *frameworks* avaliados.

Palavras-chave: UAV, MULTISPECTRAL REGISTRATION, BAND-TO-BAND REGISTRATION, BAND CO-REGISTRATION, REGISTRATION FRAMEWORK.

UAV-Multispectral Sensed Data Band Co-Registration Framework

Jocival Dantas Dias Junior

Universidade Federal de Uberlândia
Faculdade de Computação
Programa de Pós-Graduação em Ciência da Computação

Uberlândia

2020

Abstract

Precision farming has greatly benefited from new technologies over the years. The use of multispectral and hyperspectral sensors coupled to Unmanned Aerial Vehicles (UAV) has enabled farms to monitor crops, improve the use of resources and reduce costs. Despite being widely used, multispectral images present a natural misalignment among the various spectra due to the use of different sensors. The variation of the analyzed spectrum also leads to a loss of characteristics among the bands which hinders the feature detection process among the bands, which makes the alignment process complex. In this work, we propose a new framework for the band co-registration process based on two premises: i) the natural misalignment is an attribute of the camera, so it does not change during the acquisition process; ii) the speed of displacement of the UAV when compared to the speed between the acquisition of the first to the last band, is not sufficient to create significant distortions. We compared our results with the ground-truth generated by a specialist and with other methods present in the literature. The proposed framework had an average back-projection (BP) error of 0.425 pixels, this result being 335% better than the evaluated frameworks.

Keywords: UAV, MULTISPECTRAL REGISTRATION, BAND-TO-BAND REGISTRATION, BAND CO-REGISTRATION, REGISTRATION FRAMEWORK.

List of Figures

List of Tables

Acronyms list

BPE Back Projection Error

BRISK Binary Robust Invariant Scalable Keypoints

CC Correlation Coefficient

DEM Digital Elevation Model

FAST Features from Accelerated Segment Test

GA Genetic Algorithms

GCP Ground Control Points

GDP Gross Domestic Product

HSF Harris-Stephens Features

KAZE Kaze Features

MEF Min Eigen Features

MSER Maximally Stable Extremal Regions

MST Maximum Spanning Tree

NDRE Normalized Difference Red Edge Index

NDVI Normalized Difference Vegetation Index

NNS Nearest Neighbor Search

NMI Normalized Mutual Information

NSCT Non-Subsampled Contourlet Transform

ORB Oriented FAST and rotated BRIEF

PA Precision Agriculture

PCC Pearson's Correlation Coefficient

RANSAC Random Sample Consensus

RMSE Root Mean Squared Error

SIFT Scale Invariant Feature Transform

SURF Speeded-Up Robust Features

UAV Unnamed Aerial Vehicle

VI Vegetation Index

VRA Variable Rate Application

Contents

I hereby certify that I have obtained all legal permissions from the owner(s) of each third-party copyrighted matter included in my thesis, and that their permissions allow availability such as being deposited in public digital libraries.

Jocival Dantas Dias Junior

CHAPTER **1**

Introduction

Historically agribusiness has contributed about a fifth of Brazil's Gross Domestic Product (GDP). In 2018, according to data from the Ministry of Agriculture, Livestock and Supply, this sector represents 21.6% of GDP, representing in financial values R$ 570.31 billion reais. Of this amount, agriculture was responsible for R$ 383.97 billion reais (AGRICULTURA, 2019). With this information, it is clear that agribusiness is of great importance for the development of the country, being responsible for one in three jobs. Considering the global market, Brazil is also a leader in the production and export of several products, as seen in Table 1.

Table 1 – Brazil's position in the world agricultural market in 2017, adapted from (AGRICULTURA, 2019).

Main products	Brazil - World Ranking	
	Production	Exports
Sugar	1st	1st
Coffee	1st	1st
Orange juice	1st	1st
Beef	2nd	1st
Chicken	2nd	1st
Corn	3rd	3rd
Soybeans	2nd	1st
Soybean meal	4th	2nd
Soy oil	4th	2nd
Cotton	4th	2nd
Pork	4th	4th

Despite the optimistic scenario, the continued expansion of agricultural development comes up against social and ecological aspects, since the growing demand for land has caused social conflicts and degradation of the environment. Agriculture can be seen as an economy of scarce resources. Note in Table 2, that there are only 6.7% of the area available for agricultural expansion (56.6 million hectares) in the Brazilian territory. Therefore, we can see the need to increase productivity in the same planted area. According to (FILHO,

2016), an increase of 100% in the gross income of agriculture can be explained by the following factors: technology (68%); work (23%) and land (9%).

Table 2 – Land use in millions of hectares and availability in Brazil, adapted from (AGRI-
         CULTURA, 2019).

Territorial Distribution (2018)	Hectares	Percentage
Agriculture in production	**244.5**	**28.7%**
Grains	62.5	7.3%
Livestock (Pastures)	158.6	18.6%
Forests Planted with Forest Essences	8.5	1.0%
Sugarcane	8.6	1.0%
Banana, Coffee, Cassava, Cocoa, Citrus, other permanent	6.3	0.7%
Areas Protected by legislation	**5480**	**64.4%**
Conservation Units - UC	133.0	15.6%
Indigenous Lands - TI	121.0	14.2%
Legal Reserve and Permanent Preservation Areas	268.0	31.5%
Cities, Roads, Hydroelectric, other	26.0	3.1%
Areas Available for Agriculture	**56.6**	**6.7%**
Others	**1.9**	**0.2%**
Brazilian territorial area	**851**	**100%**

In this context, of demand for growth in production and pressure to minimize social and environmental impacts, Precision Agriculture (PA) proved to be the solution for the sustainable development of agribusiness. With the basic premise of producing more using fewer resources (water, land and agricultural inputs), PA has become necessary at all scales of production (from family farming to large landowners) (SCHRIJVER; POPPE; DAHEIM, 2016).

Among all PA technologies, Variable Rate Application (VRA) (tillage, seeding, fertilizing, irrigation, and pesticide application), soil mapping, automatic guidance, yield monitoring mapping, and autonomous vehicles (LIN et al., 2019) stand out. Remote sensing techniques, mainly with the use of UAV for the acquisition process, have become increasingly present for PA activities. To use VRA technology, most of the time, it is necessary to calculate indexes, such as the Normalized Difference Vegetation Index (NDVI) and the Normalized Difference Red Edge Index (NDRE). To calculate these indexes, multispectral images of the area are required, which in most applications are obtained by UAVs.

Using UAVs for image acquisition in PA requires hundreds and in some cases thousands of overlapping images to cover an area. After acquiring aerial images, it is recommended to carry out the registration process for better extraction of agronomic characteristics. In RGB images the registration process presents some difficulties that are easily identified and solved, such as changes in lighting, rotations, and changes in scale from unforeseen events along the UAV path. However, in addition to the previously mentioned problems

for RGB images, most multispectral cameras use different physical sensors to obtain different spectra, which causes a spatial misalignment among the spectra due to their physical displacement. The variation of the analyzed spectrum also leads to a loss of features among the bands which hinders the process of detection of common features between bands.

1.1 Problem Description

A multispectral or hyperspectral image to be useful for agricultural applications must first have its bands aligned. This process is known as band co-registration and it presents a series of difficulties to be carried out.

The first major difficulty in performing the band co-registration is the fact that each element present in the image is represented differently in each spectrum due to its chemical and physical characteristics, and the processes of emission, absorption, reflection, and transmission will occur with varying intensity for each region of the spectrum. This fact hampers the alignment process because, among the spectra, there is a loss of information (features) (BANERJEE; RAVAL; CULLEN, 2018).

The vast majority of multispectral cameras use different sensors to obtain the spectra. If these cameras are placed on a fixed platform, only the physical displacement among the sensors are responsible for causing misalignment among the bands. However, when coupled in a UAV, this problem is intensified. During a flight, a UAV has three basic control axes: yaw, pitch, and roll (see Figure 1). During an image acquisition process, several factors influence the direction of an aircraft (eg UAV speed, wind speed, wind direction) leading to distortions of translation, scale, and rotation among the sensors (BANERJEE; RAVAL; CULLEN, 2018).
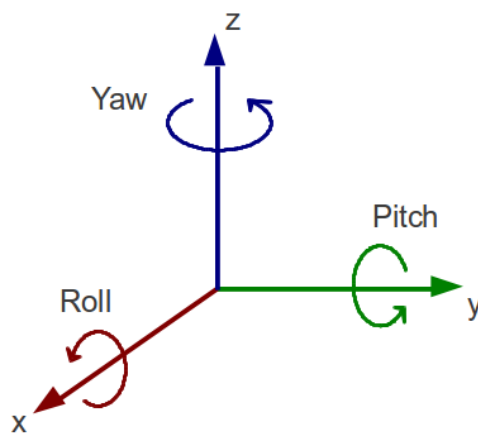
Figure 1 – Aircraft principal axes.

For PA's success, the band co-registration process is required to correct all-natural misalignment (originating from the sensor architecture) and those created during the ac-

quisition process. Therefore, the objective of this work is the development of a framework for the band co-registration process in multispectral images obtained by UAVs.

1.2   Hypothesis

Most of the works published on band co-registration in images obtained by UAVs start from the principle that it is necessary to obtain a different transformation in each image to correct the misalignment between the sensors. Going in opposition to this current, this work is based in two hypotheses:

1. Natural misalignment is an attribute of the camera, so it does not change during the acquisition process.

2. The speed of displacement of the UAV when compared to the speed between the acquisition of the first to the last band, is not sufficient to create significant distortions.

1.3   Contributions

The main contributions that this work presents are:

1. Creation of two databases with 1910 images for the band-to-band registration process. Each image was manually marked with 12 points in each band by an expert.

2. Development of a framework for the band co-registration in multispectral images obtained by UAVs.

1.4   Thesis Organization

This dissertation is structured in six chapters and a brief description of each chapter is presented below:

❏ Chapter 02 - Fundamentals: presents the concepts of precision agriculture, remote sensing and the concepts of image registration which are important to understand this work;

❏ Chapter 03 - Related Works: presents the state of the art for the band co-registration process. This chapter consists of works that are focused on the alignment of bands obtained by multispectral or hyperspectral cameras coupled in UAVs;

❏ Chapter 04 - Methodology: presents the datasets used in this work, describes the proposed framework and also presents the metrics used for the work evaluation;

❏ Chapter 05 - Experimental Results: the results obtained in each dataset, when compared to the ground-truth and the other analyzed frameworks, are presented. Discussions and comparisons between the proposed framework and the others are presented;

❏ Chapter 06 - Conclusion: presents the conclusions of the work, its results, its limitations, and future work.

CHAPTER **2**

Fundamentals

2.1   Precision Agriculture

The main discussion of the future of agriculture shows that food production must increase dramatically - probably doubling by 2050 - while using only 5% more land to sustain the growth of the world's population (HUNTER et al., 2017). Projections shows that by 2050 the world's population is expected to be close to 10 billions of people (HUNTER et al., 2017) (Figure 2). However, with environmental changes, this increase in food production must be made most smartly, that is without depleting natural resources or leveraging climate change, this is the main challenging in modern agriculture.
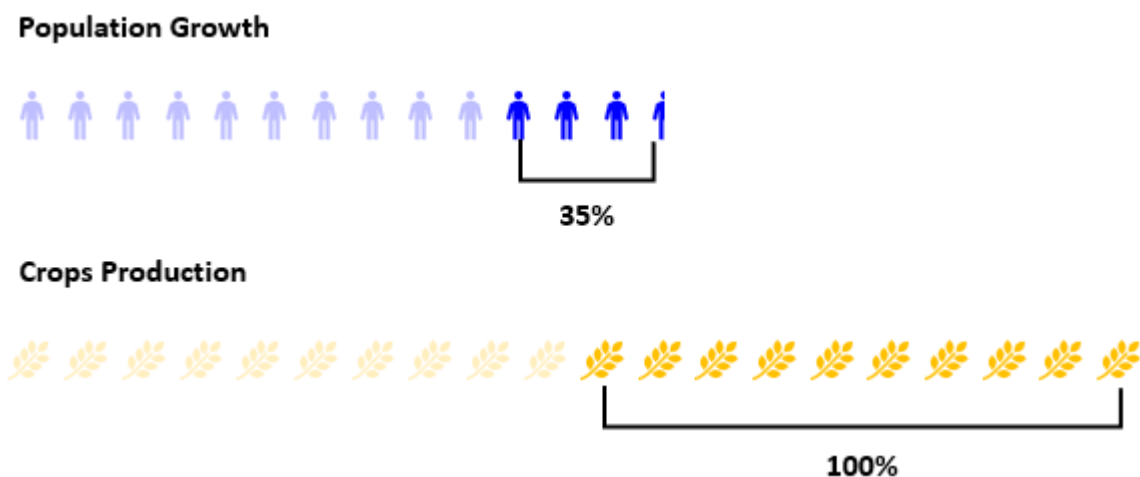
Figure 2 – Comparison between the population growth and the needed growth in crop productions to feed population at 2050.

For this reason, a new movement called PA emerged in United States in the early 1980s with the purpose to increase the quality and quantity of agricultural output while using less input (energy, fertilizers, pesticides, water, etc), i.e., to produce more and better food while reducing environmental impact and saving costs (SCHRIJVER; POPPE; DAHEIM,

2016). The PA methods rely mainly upon a combination of remote sensing, automation, robotics, big data, artificial intelligence, and the internet of things technologies.

Different from the traditional agriculture that treats the fields homogeneously, the PA divides the fields into management zones which are treated individually, thus receiving the inputs as needed for each zone. As stated before, this results in an increasing financial return to farmers, as the number of inputs is applied to a lesser extent while productivity remained or increased (MAES; STEPPE, 2019).

According to (TARABELLA; TRIVELLI; APICELLA, 2019), the implementation of PA can increase, in average, total profitability from \$55 to \$110 per acre (1 acre = 4046.87 m^2). However, in Italy, only 1% of the cultivated agricultural area uses the means and technologies of PA (TARABELLA; TRIVELLI; APICELLA, 2019).

PA is widely recognized as the third revolution of modern agriculture. The first revolution of modern agriculture was the introduction of mechanization (1900 to 1930), the second one was the genetic modification (1990 to 2005) (GLOBAL, 2017). Figure 3 illustrate the average of how many people a single United States farmer fed, in the same acreage, along a certain period in time.

Figure 3 – Average of how many people a single United States farmer fed in the three main agricultural revolutions.

2.1.1 Unmanned Aerial Vehicles

The use of UAVs in agriculture started in the early 21st century. In the 2000s, the satellites provided images with bad spatial and temporal resolutions which causes incorrect analyzes that leads to waste of agricultural inputs and delay on the data acquisition process (MILICS, 2019). These images are mostly used to obtain an overview of the field. The next method for obtaining images used has airplanes and balloons, which provided better temporal and spatial resolutions. However, the cost of the acquisition process was too expensive for agricultural applications (MILICS, 2019). Nowadays, the use of UAVs became accessible to the majority of the farmers, which led to a growth of the studies in PA that uses UAVs. According to (MAES; STEPPE, 2019), the number of studies using UAVs in precision agriculture has exponentially increased in the last 8 years.

The unmanned aerial vehicles can be divided into two main classes, multi-rotor, and fixed-wing aircraft. Each of these classes has vantages and disadvantages, especially con-

cerning area coverage, flight time, accessibility, payload capacity, price and take-off, and landing requirements (DRONEDEPLOY, 2017).

Multi-rotor is the most common type of UAV for making models and maps for the PA. Normally, this type of aircraft has a central body and multiples rotors that power propellers to maneuver the aircraft and take flight. Generally, the multi-rotor are quadcopters but they can have six or eight rotors (hexacopter and octocopter, respectively). The multi-rotor UAV controls the vehicle motion by changing the relative speed of each rotor, this allows this kind of UAV to make a unique range of movements (DRONEDEPLOY, 2017). Figure 4 shows examples of multi-rotor aircraft.

Figure 4 – Example of DJI multi-rotor UAV, from (DRONEDEPLOY, 2017).

Fixed-wing is more similar to an airplane, they have a central body that has two wings and normally one propeller. However, this kind of aircraft is more atypical outside agriculture applications (DRONEDEPLOY, 2017). Figure 5 shows an example of a fixed-wing aircraft.

Both of these types of UAVs has some advantages and disadvantages. The main advantages of multi-rotor drones are greater maneuverability, more compact, ease-of-use, higher payload capacity and normally they have lower prices than fixed wings. The fixed wings present a significant range, safer recovery of a motor power loss, linear flight advantage and greater stability (DRONEDEPLOY, 2017). Figure 6 shows the comparison of the multi-rotor and fixed wings in some aspects.

Figure 5 – Fixed wing UAV SX2 by Sensix Innovations.

Figure 6 – Summary comparison between Multi-rotor and Fixed-wing aircrafts, from (DRONEDEPLOY, 2017).

2.1.2   Remote sensing in Precision Agriculture

Remote sensing can be defined as the acquisition of information about an object without making physical contact, i.e., by using land platforms, satellites, and/or aircraft (ZARCO-TEJADA et al., 2016). In PA, it can be defined as the process of capture field-level data.

At the beginning of PA, the remotely sensed images were only obtained by satellites, airplanes or helicopters. These processes, besides being expensive, did not provide the data fast enough for the optimal use of PA methods. However, in the last decade, the

development of UAVs initialized a new era in the PA, since this equipment provides data of an unprecedented spatial, spectral, and temporal resolution (MAES; STEPPE, 2019).

Remote sensed imagery has several uses in PA, e.g., classification of crop species (DYR-MANN; KARSTOFT; MIDTIBY, 2016), monitoring of crop diseases and weeds (PICON et al., 2019), detection of crop water stress (IHUOMA; MADRAMOOTOO, 2017) and mapping soil properties. However, some issues must be evaluated before using the remotely sensed images for the process of decision-making in PA, since several parameters are affected by the type of platform (satellite, air or ground) and the sensor chosen for the data acquisition: (i) geometric precision of the images; (ii) radiometric; (iii) spectral; (iv) spatial; (v) temporal resolution; (vi) the width and number of spectral bands obtained by the sensor; (vii) the quality of spectral information represented in the images. These parameters influence the quality of remote sensed images and future analysis (see Figure 7) (KHANAL, 2017).
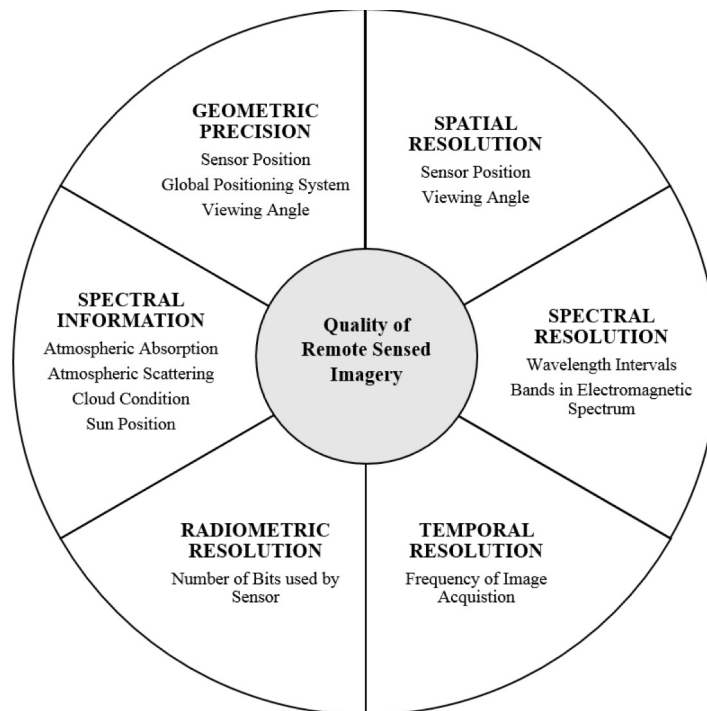
Figure 7 – Quality factors in remote sensing, from (KHANAL, 2017).

2.1.2.1 Quality in Remote Sensing

As stated earlier, the quality of information extracted from remotely sensed imagery depends on four types of resolution, i.e., temporal, spatial, spectral and radiometric. In this section, we will explain each one and its influence on the image.

One important resolution that leads farmers to choose UAVs instead of satellite images is the temporal resolution and it can be defined as the quantity of time needed to reacquire images from the same location (e.g. field) (THÉAU, 2008). A higher temporal resolution

<table>
<tr><td>(a) Lower Spatial Resolution.</td><td>(b) Higher Spatial Resolution.</td></tr>
</table>
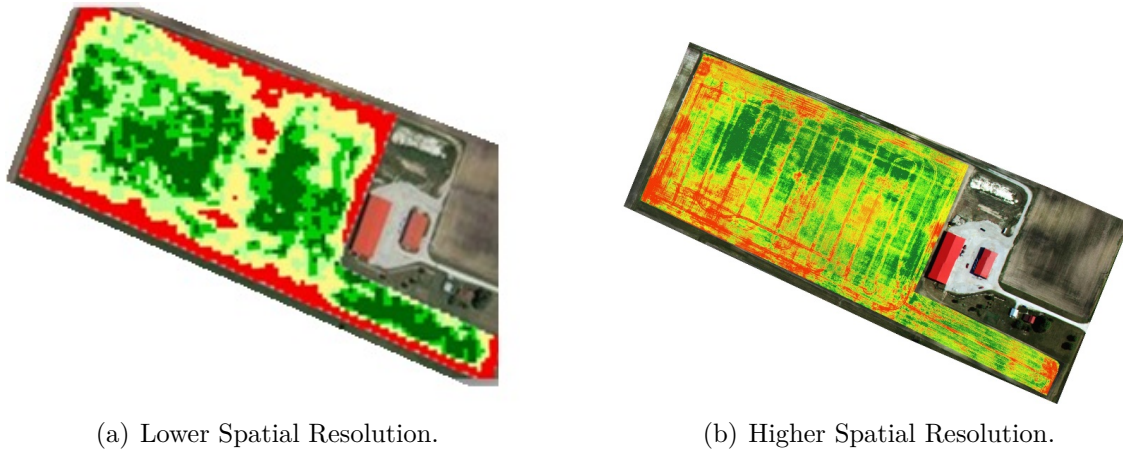
Figure 8 – Comparison of vigor map in (a) has a ground sampled distance of 10 meters and (b) has a ground sampled distance of 0.25 meters, from (KHANAL, 2017)

means a lower delay between one acquisition from another in the same location and vice-versa.

The UAV remote sensed imagery has higher temporal resolution than satellites. This is because, generally, the satellites have a resolution varying in days (e.g., the Landsat-8 and MODIS that have, respectively, 16 and 1 days of temporal resolution (HAZAYMEH; HASSAN, 2015)) while to obtain new data with the use of UAVs it is only necessary to perform a new flight over the desired area, which, in most cases, will take only a few hours to be performed. The temporal resolution is very important for precision agriculture since most methods require immediate analysis of the fields for the decision making process.

When referring to pixel size, the spatial resolution specifies the smallest detectable feature in the image. In other words, it can be defined as the ability to distinguish the smallest details. In images with a high spatial resolution, even the smallest object can be recognized, and this will lead to better feature extraction of the image. However, in images with lower spatial resolution, a single-pixel will represent multiples features, and this will make the process of distinguishing a feature from another difficult (KHANAL, 2017).

Generally, the UAV remote sensed imagery has a higher spatial resolution than the satellite imagery. This is mainly caused by the lower altitudes that the UAV acquired the image. Figure 8 shows the difference between the generated map of the vigor of a crop with higher and lower resolution.

Spectral resolution can be defined as the length of the continuous wavelength that can be detected by a sensor in the electromagnetic spectrum. In other words, it means the range of electromagnetic spectrum and the number of spectral bands that can be measured by a sensor (Khan et al., 2018). Figure 9 shows the LANDSAT TM and TERRA Aster firsts bands and their spectral resolution. Figure 9 demonstrate an example of the difference in spectral resolution between two satellites, channel 3 of TERRA Aster corresponds to a narrower range that is centered on a different value than the near-infrared

of LANDSAT TM channel 4. For channel 4 of TERRA Aster and 5 of LANDSAT TM, the bandwidth is also narrower. Between 2.05 and 2.35 µm, the sensors have different designs: Terra Aster achieves four channels (5 to 8) and LANDSAT TM integrates the wavelengths in one single spectral measure (channel 7) (OSE; CORPETTI; DEMAGISTRI, 2016).
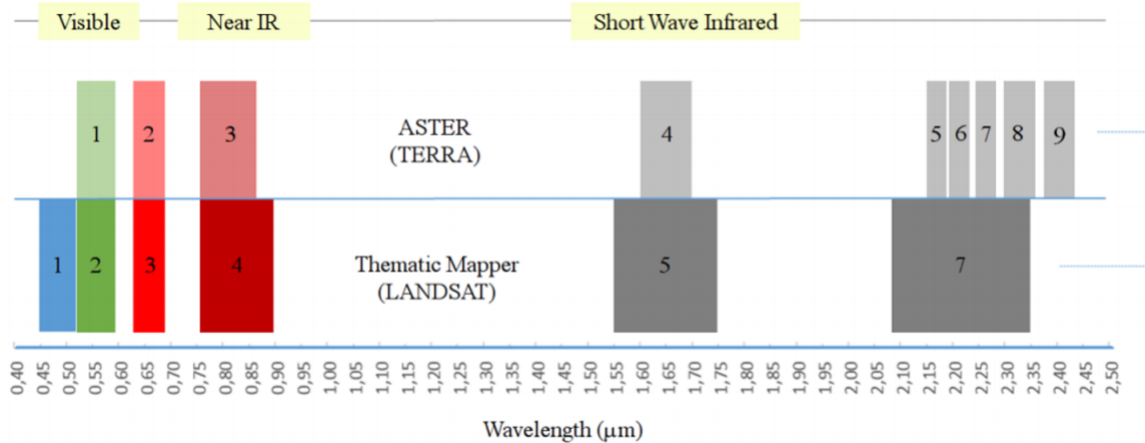
Figure 9 – LANDSAT TM and TERRA Aster firsts bands and their spectral resolution, from (OSE; CORPETTI; DEMAGISTRI, 2016)

Remote sensing imagery with a higher spectral resolution is better for the PA methods because a large number of spectral bands with a lesser range of wavelength lead to better features for several applications, e.g., crop disease detection and biomass estimation (KHANAL, 2017).

Radiometric resolution is the sensitivity of the sensor, i.e., its ability to measure and to distinguish slight variations in the electromagnetic energy emitted or reflected by the elementary ground surfaces. In remotely sensed imagery, data is recorded as a positive digital number (DN) which range of 0 to $2^n - 1$, where n depends on the number of bits that the sensor uses to represents spectral data (OSE; CORPETTI; DEMAGISTRI, 2016)(KHANAL, 2017). Figure 10 shows the difference between an image with low and high radiometric resolution.
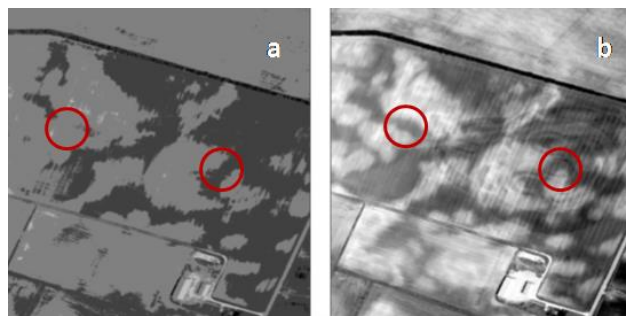
Figure 10 – Example of the difference in the level of details in two radiometric resolutions (a) represents the red band with 2 bits and (b) represents the red band with 16 bits, from (KHANAL, 2017)

The higher the radiometric resolution is, more strong are the differences between the information represented in images. It leads to a higher sensitivity to detect minor differences in images.

In addition to the four resolutions explained, two factors are also of great importance for remote sensing quality, namely: geometric correction and radiometric calibration/correction. Remotely sensed images obtained by satellites, UAVs or aircraft, are generally geometrically distorted due to the movements of the platform and the acquisition process. Many factors influence geometric distortion in remotely sensed images (e.g. earth rotation, position and dynamic state of the platform and topographic relief) (TAWFEIK; HAMZA; SHAWKY, 2016). Specifically, in images obtained by UAVs, this geometric distortion is accentuated due to factors such as low UAV stability, wind speed, wind direction, and flight plan problems.

The process of rectification of the geometrically distorted image is commonly called ortho-rectification and it is the first and main step before images can be used in any application (KHANAL, 2017). The traditional method for ortho-rectifying images consists of complex photogrammetric equations that make mathematical relations between the target, the image, and the sensor. These equations normally need parameters like focal length, lens distortion, the altitude of the sensor and terrain elevation.

To validate the quality of ortho-rectified images Ground Control Points (GCP) are commonly used. GCP are points on the earth's surface with known locations and easily distinguishable. If the location does not have natural GCP, white metal sheets can be placed into several locations and their coordinates storage to establish a relationship between the coordinates of the image and the coordinates of the terrain (KHANAL, 2017).

Some studies try to automate the ortho-rectification process in images obtained by UAVs. These methods rely on sensor's parameters (sensor size, pixel resolution, and focal length), UAV coordinates and the high overlap between the images (approximately 80%).

Radiometric calibration can be defined as the process of converting pixel intensities (i.e. DN) into physical parameters (i.e., spectral reflectance). The radiometric calibration in images obtained by UAVs is generally made with a reflectance panel with known reflectance values. Images of the reflectance panel are taken before the flight over the fields using the same sensor mounted on the UAV. The images of the reflectance panel are lately used to improve accuracy (KHANAL, 2017).

2.1.3   Sensors

The main reason for applying UAVs in precision agriculture is to obtain high-quality images. Therefore, sensors represent a fundamental part of the majority of precision agriculture applications. Choosing the sensor depends on several factors, for example, spatial resolution, spectral resolution, optical quality, the sensor's weight, and the price (MILICS, 2019).

The first kind of sensor used in precision agriculture were regular commercial RGB (red-green-blue) cameras and/or in regions near the infrared (HUNT et al., 2010). The newly developed sensors bring to the UAV the possibility of obtaining multispectral and hyperspectral images (BERNI et al., 2009).

2.1.3.1 Visible Light Sensors

Visible light sensors capture the red, green and blue (RGB) channels of the visible light. The commercial RGB sensors although they are cheap and have a high spatial resolution, have a poor spectral resolution. Usually, these cameras are used to calculate some Vegetation Index (VI) and to generate high-resolution Digital Elevation Model (DEM) (MAES; STEPPE, 2019). Figure 11 shows an example of Visible Light Sensor.

Figure 11 – MAPIR Survey2 Camera - Visible Light RGB by MAPIR.

2.1.3.2 Near Infrared Sensors

Currently, RGB cameras have been modified to replace the green filter with an infrared filter (RGN), making these modified cameras sensitive to the near-infrared spectrum (NIR) (MAES; STEPPE, 2019). For the precision agriculture methods, the wavelength of the electromagnetic spectrum between 720 and 1,000nm is very important to calculate various indices that demonstrate the state of the vegetation (MAES; STEPPE, 2019). It is also important to note that the red-edge band (around 680–730nm) is also used in these indices. Figure 12 shows an example of RGN filter.

2.1.3.3 Multispectral Sensors

Multispectral and hyperspectral sensors have multiple channels and they collect data in different ranges or specific wavelengths of the electromagnetic spectrum. The main difference between the multispectral cameras when it's compared to the RGB cameras

Figure 12 – MAPIR Survey3W Camera - red+green+nir (RGN, NDVI) by MAPIR.

is the fact that the multispectral sensors use a different sensor for each channel (MAES; STEPPE, 2019). The main multispectral cameras are a combination of sensors responsible for obtaining red, green, blue and other spectra such as near-infrared (nir) and red-edge (rededge). Figure 13 shows an example of multispectral camera.
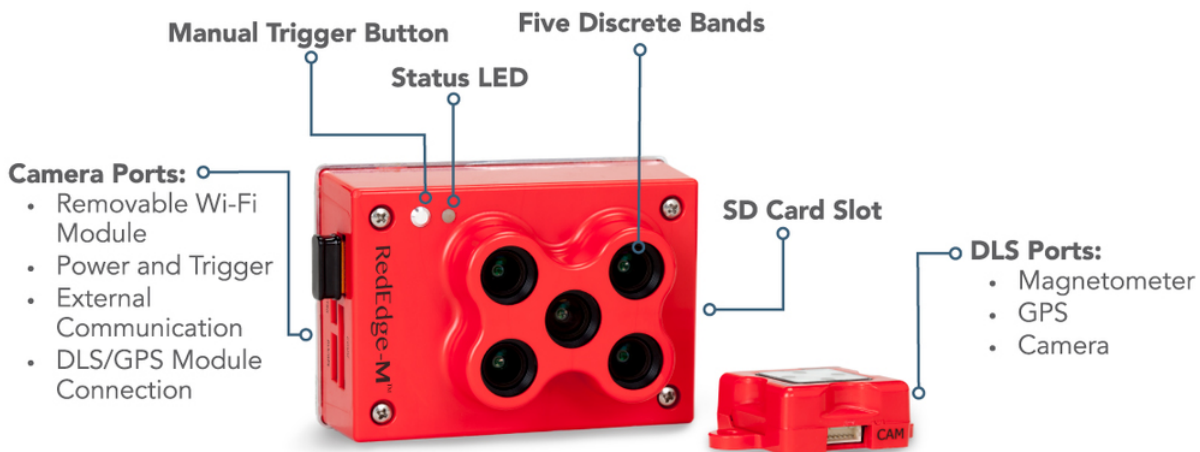
Figure 13 – MicaSense Red-Edge camera by MicaSense.

The main difference between multispectral and hyperspectral imagery is the spectral resolution. When compared to the multispectral images, which deal with fewer bands, the hyperspectral images combine thousands of fine wavelength intervals to provide detailed information.

2.2   Image Registration

The Image Registration process can be defined as the task of aligning two or more images. This process requires the definition of an image to be used as a reference and the application of geometric transformations (e.g. translations, rotations, and scale) in the other images to align with respect to the reference image. Misalignment between images

can be caused by different reasons, such as distortions among the sensors used to obtain them and changes in camera pose.

According to (HONG; ZHANG, 2008), image registration is the process of geometrically aligning an image on another image of the same scene taken from different points of view or by different sensors. It is one of the main image processing techniques and is important for several applications (e.g. integrating information obtained by different sensors, finding differences in images obtained in different periods, three-dimensional reconstruction, among others).

2.2.1 Image Registration process

According to (HONG; ZHANG, 2008), the feature-based image registration process can be divided into four steps (see Figure 14):

I Extraction of Features, which identifies relevant control points between the two images;

II Feature matching, which establishes the correspondence between the control points of the images;

III Construction of the mapping function;

IV Image Transformation
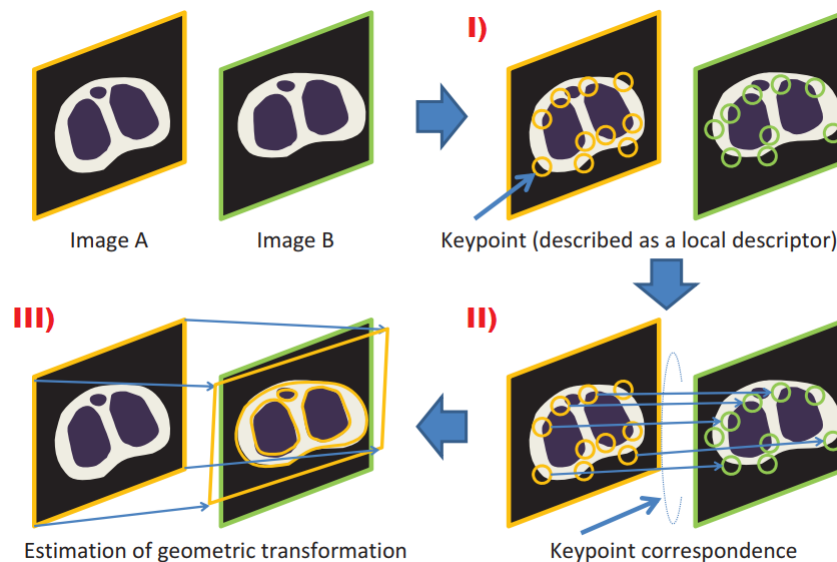
Figure 14 – Example of the steps required to register images using control points. I) Extraction of features from the images. II) Feature matching. III) Construction of the mapping function and image transformation. (Adapted from (UCHIDA, 2013))

2.2.1.1   Features Extraction

Features can be defined as a pattern that occurs at one location in the image and differs from its closest neighbors. Usually, this pattern is associated with a sudden change in one or more properties of an image (e.g. texture, color or intensity) (KUMAR; SREEKUMAR, 2014) (TUYTELAARS; MIKOLAJCZYK et al., 2008). Algorithms for image registration based on keypoints find these points by analyzing the magnitude and direction of the intensity changes in the local neighbors of the image to detect regions, corners, and borders (LOWE, 2004). Figure 15 shows the control points detected by the KAZE Features technique in an image. The points are shown with a circle centered on them. The radius of each circle represents the scale of each control point and the line in the center of each circle represents the orientation of the control point.
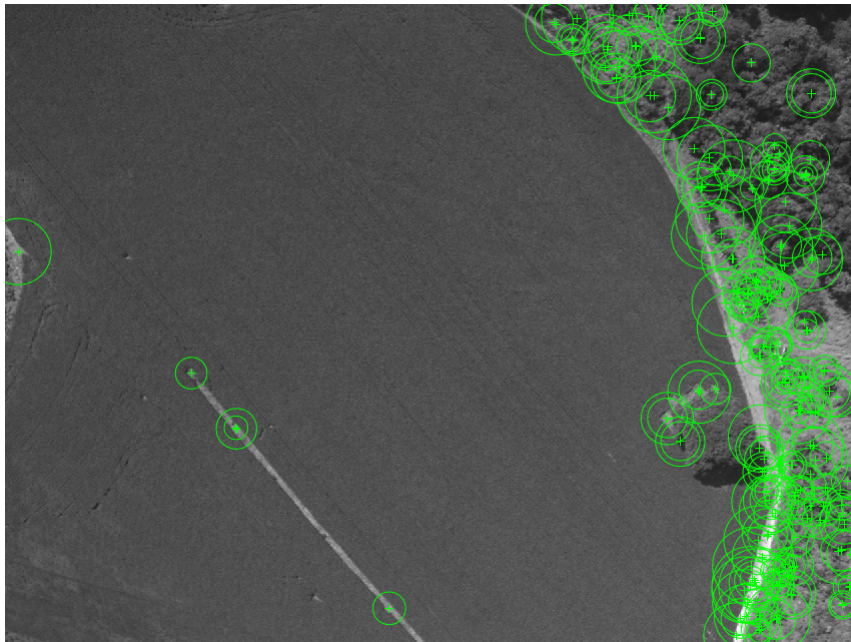
Figure 15 – Example of control points in an image.

2.2.1.2   Feature matching

After extracting the control points, it is necessary to create a correspondence between the points obtained in each of the images. Exhaustive (e.g. brute force) and approximate (e.g. Nearest Neighbor Search (NNS) (MUJA; LOWE, 2009)) methods can be applied to obtain matches.

In the brute force method, for each control point obtained in the first image, a distance measurement (Hamming for binary features and Euclidean for others) is calculated for all points obtained in the second image. This method seeks to find the closest correspondence for each point analyzed. Despite obtaining good results, this method is computationally expensive due to the excessive number of comparisons.

As described in the work of (MUJA; LOWE, 2009), depending on the application and the required accuracy, approximate methods can be used to obtain the correspondences between the points. The authors also prove that the approximate methods proposed by them reduce the execution time by several orders of magnitude when compared to linear searches.

Algorithms for obtaining control points can extract thousands of points in images obtained by UAVs. For this reason, it may also be necessary, in addition to the feature matching step, to apply techniques for removing outliers, which in the context of control points, can be defined as the inaccurate match of a pair of control points, such as the D'Lowe (LOWE, 2004) test. The D'lowe test, or Nearest Neighbor Distance Ratio, is a metric used to determine the best match for a feature and thus remove outliers. Basically, it consists of, given a feature f_a take two close candidates for match f_b and f_c, it is calculated: $d(f_a, f_b)/d(f_a, f_c)$, where d is a distance metric. If the result is a small value f_b is a good match, otherwise f_b is ambiguous or incorrect. D'lowe proposes in his work that the value to be used as a threshold for this metric is 0.8.

2.2.1.3 Construction of the mapping function

Mathematically a mapping function, or warping, can be defined as a 2D function that maps the $x - y$ coordinates from image A into the $x - y$ coordinates in image B (WOLBERG, 1994). There are two main types of mapping function (Linear and Non-Linear) that are characterized by the type of deformation in the image. Figure 16 exemplifies the transformations.
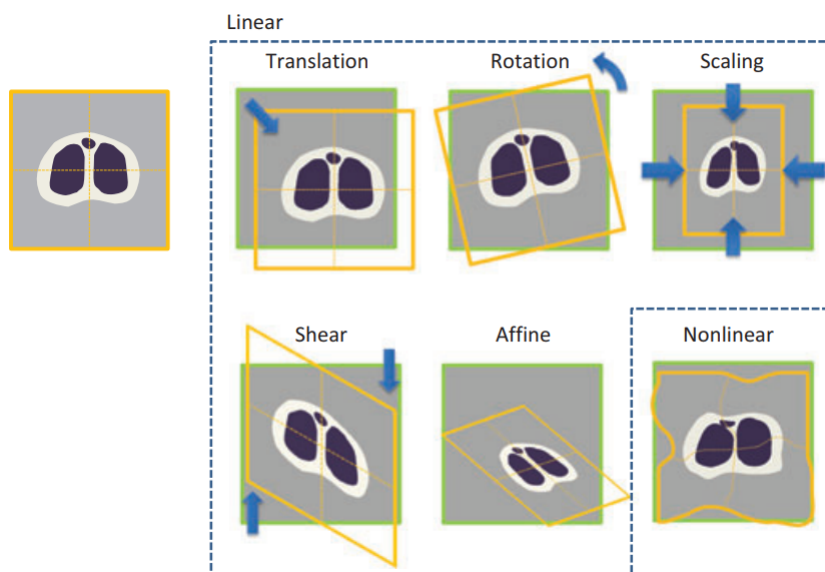
Figure 16 – Example of linear and non-linear transformations. Figure adapted from (UCHIDA, 2013).

One of the main $2D$ linear geometric transformations is the affine transformation. Related transformations include changes in scale, shear, rotations, translations, and their combinations. One of its main properties is that parallel lines remain parallel after the transformation. Linear transformations can be represented as,

$$\begin{bmatrix} X \\ Y \\ 1 \end{bmatrix} = \begin{bmatrix} a & b & e \\ c & d & f \\ 0 & 0 & 1 \end{bmatrix} \times \begin{bmatrix} x \\ y \\ 1 \end{bmatrix} \tag{1}$$

where (x, y) are the x-y coordinates of image A and (X, Y) are the coordinates of image B (reference or target). Parameters e and f represent translations on the x and y axes respectively. For rotation, $a = d = cos\ \theta$, $b = sin\ \theta$ and $c = -sin\ \theta$. As related transformations deal with all cases, the parameters a, b, c, d, e and f are arbitrary (UCHIDA, 2013).

One of the methods available in the literature for estimating geometric transformations is the Random Sample Consensus (RANSAC). RANSAC is a robust method for estimating geometric transformations, and it works as follows: first, three or more matches are selected randomly from a N amount of matches, and the parameters are defined following these selected matches. Subsequently, it is evaluated how much the remaining correspondences are in agreement with the estimated parameters. If the current parameters contain a sufficient amount of agreement between the unevaluated matches, the parameters are selected. As it does not use all correspondences to find the parameters, the RANSAC method is robust to false correspondences (FISCHLER; BOLLES, 1981) (UCHIDA, 2013).

2.2.1.4   Image Transformation

Finally, the last step to perform the registration process is to transform the image according to the transformation function obtained in Section 2.2.1.3. To transform the images according to the target image (b), the other images (a) are mapped according to the transformation obtained in Section 2.2.1.3, as shown in Figure 17.

2.2.1.5   Evaluation metrics

Several techniques have been proposed to measure the quality of the registration process. Several studies have already emphasized the importance of evaluation metrics in the registration process (LEITE et al., 2011) (RAZLIGHI; KEHTARNAVAZ; YOUSEFI, 2013) (MELBOURNE; RIDGWAY; HAWKES, 2010).

One of the techniques used to assess alignment is the Root Mean Squared Error (RMSE) obtained according to the Equation 2.

$$\text{RMSE} = \sqrt{\frac{\sum_{i=1}^{N} \sum_{j=1}^{M} (P(i,j) - P'(i,j))^2}{NM}} \tag{2}$$
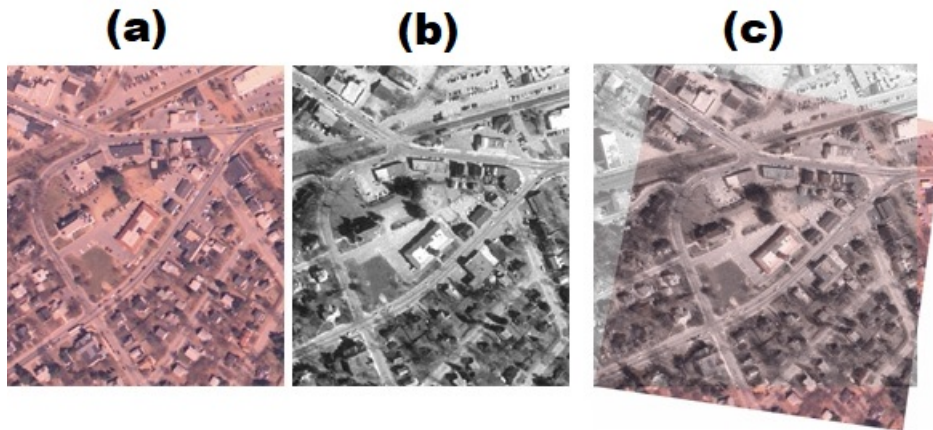
Figure 17 – Example of transforming an image (a) to the target image (b). The result of the overlay after the transformation is shown in the image (c) (MATH-WORKS, 2018).

where M and N represent, respectively, the number of lines and columns of the image, $P(i,j)$ represents the pixel in the line i and column j of the aligned image and $P'(i,j)$ represents the pixel in the i row and the j column of the registered image.

Smaller RMSE values indicate better alignment between the two images. One of the limitations of this technique is the need for a base previously aligned by a specialist to obtain a realistic assessment of performance.

Another technique used in several works is Back Projection Error (BPE). This technique represents how well the location of the target image's control points aligns with the registered image's control points. Given X_i and X_j as the same control points defined by the specialist on the, respectively, target image (i) and moving image (j), T the affine transformation matrix estimated by a method and d the euclidean distance function, the BPE can be defined as shown in Equation 3. Smaller BPE indicates better image registration performance. This technique also has the same limitation as the RMSE, to obtain real results it is necessary to use a previously aligned database.

$$\text{BPE}(I, J) = \sum_{x_i, x_j} d^2(X_i, TX_j) \tag{3}$$

2.2.2 Control Points for Image Registration

A great deal of work in the area of image registration has been developed recently. As analyzed by (YASIR, 2018), the main focus of recent algorithms for image registration was focused on increasing the number of control points obtained in different scenes, sensors, and situations. When restricted to the multispectral registration area of images obtained by UAVs, the main algorithms are: Scale Invariant Feature Transform (SIFT), Speeded-Up Robust Features (SURF), Binary Robust Invariant Scalable Keypoints (BRISK), Min Eigen Features (MEF), Kaze Features (KAZE), Oriented FAST

and rotated BRIEF (ORB), Maximally Stable Extremal Regions (MSER) and Features from Accelerated Segment Test (FAST). A brief description of each method is presented below.

2.2.2.1   Scale Invariant Feature Transform

The SIFT algorithm was proposed by (LOWE, 2004) and it is used to detect and extract control points that are described as local features in the image. According to (ISIK, 2014) we can describe the SIFT in four stages:

1. Detection of maximum value points in the scale space;

2. Location of Control Points;

3. Guidance Assignment;

4. Control Point Descriptor.

In the first stage, the image is checked in different regions and scales to find points of interest that are invariant in the scale and orientations. These points are defined as local scale-space maxima obtained from the Difference of Gaussian (DoG), which is calculated by subtracting different Gaussian scales (ISIK, 2014).

When locating control points, insignificant points are rejected and the edge response is eliminated. While points with low contrast are rejected according to a previously defined threshold, points that are not part of the border are eliminated. To eliminate these points, SIFT uses a Hessian matrix to find the main curvatures (ISIK, 2014).

To obtain descriptors that are invariant to rotations, SIFT creates an orientation histogram from the gradient orientations at each maximum location of the DoG function in a region around the control point, usually a region of size 16×16.

The last stage is the construction of the features vector. This vector is constructed considering the direction of the control point where the gradient force is maximum. Typically the feature vector obtained by SIFT has a size of 128 elements.

Many variants of SIFT have been proposed for the most different problems. It is worth mentioning the PSO-SIFT proposed by (MA et al., 2017), which increases the amount of feature matching when used in multispectral/hyperspectral images.

In (MA et al., 2017), a new gradient definition was proposed to address the differences between the intensities of the images obtained by different sensors. Subsequently, an improved method for performing feature matching by combining the position, scale, and orientation of each control point is presented to increase the number of correct matches. The authors also performed experimental tests on multispectral and multisensory datasets. According to the authors, the proposed method presented better results when it comes to the amount of correspondence and the alignment accuracy than several other methods considered state of the art.

2.2.2.2   Speeded-Up Robust Features

SURF (BAY; TUYTELAARS; GOOL, 2006) is a scale and rotation invariant key-points detector and descriptor. In comparison with traditional methods, the SURF algorithm approximates or, in some cases, outperforms these methods in robustness, distinctiveness, and repeatability. Moreover, the SURF can be computed and compared faster than other methods (BAY; TUYTELAARS; GOOL, 2006).

The SURF technique has gained a lot of space in several study areas for the selection of features because, in addition to presenting scale and rotation invariance, the computational time of the SURF method is lower when compared to other methods of extracting features in cases of detection and correspondence between control points. SURF detects points of interest with the aid of pre-computed integral images to approximate the determinant of the Hessian matrix.

For the detection of control points, the SURF technique uses the sum of Haar's 2D wavelet around a point of interest. Haar's 2D wavelet is obtained by an approximation of the determinant of the Hessian matrix which, in turn, extracts structures in the form of regions at the location where the determinant is maximum. Subsequently, the great improvement in the performance of the SURF technique can be attributed to the non-maximal suppression of the determinants of the Hessian matrices (ISIK, 2014).

To describe the control points, the SURF algorithm first divides the region around each control point into square regions of size 4×4. Subsequently, Haar's 2-D wavelet is calculated for each sub-region, this step can be calculated with the aid of integral images. Therefore, each control point is described as a 64-dimension vector (ISIK, 2014).

2.2.2.3   Binary Robust Invariant Scalable Keypoints

Although techniques such as SURF and SIFT obtain good results and they are invariant to various types of transformations (e.g. scale, rotations and changes in the point of view) when analyzing the performance we see that these techniques are extremely computationally expensive. In this context, the BRISK was proposed by (LEUTENEGGER; CHLI; SIEGWART, 2011) to be an algorithm with high performance, however, with a drastic reduction of the computational cost when compared to algorithms like SIFT or SURF.

As (ISIK, 2014), the BRISK technique proposed by (LEUTENEGGER; CHLI; SIEGWART, 2011) uses the AGAST Corner Detector (MAIR et al., 2010) technique, which holds a performance improvement over the FAST algorithm. This method can be divided into three main parts:

1. Sample Pattern;

2. Orientation Compensation;

3. Sample Pairs.

The sampling pattern around the control points in the BRISK algorithm represents some points spread over several concentric circles, which are used to define whether a point is a corner or not. To determine if a point is a corner, the FAST (ROSTEN; DRUMMOND, 2006) detector is used. The points are then separated into two sets: short distance points and long-distance points (ISIK, 2014).

To obtain the rotation invariance, the direction of each control point is determined by obtaining the sum of the local gradient between the even points of long-distance and those of short distance. Subsequently, all points are rotated according to the guidelines obtained (ISIK, 2014).

In the end, the intensity of the first point and the second point in the pair is compared. If the intensity of the first point is greater than that of the second, the algorithm returns 1; otherwise, it returns 0. So, after comparing all the 512 points, the descriptor will be determined by a 512 bit array. To perform the comparison between the descriptors, the Hamming distance is used instead of the Euclidean distance, as the Hamming distance uses only the sum of the XOR operation between the bits of two vectors, which improves the performance considerably (ISIK, 2014).

2.2.2.4   Harris Corner Detector

The Harris corner detector (HARRIS; STEPHENS, 1988) is a technique for locating keypoints in images. It is widely used in several practical applications such as camera calibration, tracking, image matching, and video stabilization. This method is based on the Moravec's detector, which is based on the auto-correlation function of the image for measuring the intensity differences between a patch and windows shifted in several directions (SÁNCHEZ; MONZÓN; NUEZ, 2018). Its success is due to its efficiency and its simplicity of implementation. Your method can be summarized in the following steps:

❏ Consider I the image, compute x and y derivatives of image (with Sobel operator):
$I_x = G_\theta^x * I$
$I_y = G_\theta^y * I$

❏ Compute products of derivatives at every pixel:
$I_x^2 = I_x * I_x$
$I_y^2 = I_y * I_y$
$I_x y = I_x * I_y$

❏ Compute the sums of the products of derivatives at each pixel:
$S_x^2 = G_{\theta'} * I_x^2$
$S_y^2 = G_{\theta'} * I_y^2$
$S_x y = G_{\theta'} * I_x y$

❑ Define at each pixel (x, y) the matrix:

$$H(x, y) = \begin{bmatrix} S_x^2 & S_x y \\ S_x y & S_y^2 \end{bmatrix}$$

❑ Compute the response of the detector at each pixel:

$R = Det(H) - k(Trace(H))^2$ where

$Det(H) = \lambda_1 * \lambda_2$

$Trace(H) = \lambda_1 + \lambda_2$

λ_1 and λ_2 are the eigenvalues of H.

The R score is analyzed for each window to determine whether this window is flat, edge or a corner. The classification rule is as follows:

❑ When $|R|$ is small, the region is flat.

❑ When $R < 0$, the region is an edge.

❑ When R is large, the region is a corner.

At the end of the process, the Harris Corner Detector will have a grayscale image with the R scores. Thresholding the R scores will return the corners of the image.

2.2.2.5 Shi-Tomasi Corner Detector (Min Eigen Features)

MEF are obtained by using the Shi-Tomasi Corner Detector algorithm. This algorithm was proposed by (SHI; TOMASI, 1994) and it is based on the Harris Corner Detector (HARRIS; STEPHENS, 1988) algorithm with a small change in the selection criteria.

As shown in Section 2.2.2.4, the formula for determining whether or not a corner exists in the Harris corner detector can be expressed by: $R = \lambda_1 * \lambda_2 - k(\lambda_1 + \lambda_2)^2$. Instead, Shi-Tomasi proposed the following change to this formula: $R = min(\lambda_1, \lambda_2)$, that is, he is only evaluating eigenvalues.

As analyzed in (SHI; TOMASI, 1994), this change proved to be experimentally superior to the selection criterion proposed in the Harris Corner Detector algorithm. In addition to having a better selection method, this algorithm is also invariant to changes in lighting, scale, and speed.

2.2.2.6 Kaze Features

The KAZE algorithm was proposed by (ALCANTARILLA; BARTOLI; DAVISON, 2012) to detect 2D characteristics in non-linear scale-space to obtain greater accuracy of location and distinctiveness.

The Gaussian blurring method that is used to generate the scale space in other algorithms does not maintain the natural edges of the analyzed image and the noise is also

smoothed at all levels of scale. To solve this problem, the KAZE algorithm uses non-linear diffusion filtering together with the AOS (Additive Operator Splitting) (ANDERSSON; MARQUEZ, 2016) method. The KAZE algorithm presents illumination, scale and rotation invariance.

2.2.2.7   Oriented FAST and rotated BRIEF

ORB was proposed by (RUBLEE et al., 2011) and it was developed to be a very fast binary descriptor based on BRIEF with rotation invariance and noise resistance.

This method consists of detecting control points using FAST for this purpose. FAST does not present a quality measure for the corners detected. For this reason, the Harris corner measure (HARRIS; STEPHENS, 1988) (HCM) was used to sort the keypoints obtained by FAST. A threshold is applied to select only the N best keypoints. FAST also does not produce multi-scale features, so a scale pyramid of the image and features (filtered by Harris) is generated at each level of the pyramid. By default, FAST also does not have an orientation component in its points. For this reason, the ORB uses the centroid intensity as a measure to determine the orientation of the corner (RUBLEE et al., 2011).

For its descriptors, the ORB uses the BRIEF method, which is a binary descriptor. However, originally the BRIEF method is not invariant for rotations, for this reason, the Rotation-aware BRIEF (rBRIEF) was developed, making it invariant to rotations. According to tests demonstrated in (RUBLEE et al., 2011), the ORB obtained a performance in two orders of magnitude greater than the SIFT. In addition, it obtained good results in several situations in the real world.

2.2.2.8   Maximally Stable Extremal Regions

MSER is a method proposed by (MATAS et al., 2004) for blob detection in images. Similar to SIFT, MSER extracts from an image some co-variant regions, which are called MSERs. MSER regions can be defined as connected areas that are characterized by an almost uniform intensity and surrounded by a constructive background. They are constructed through a process of trying multiple thresholds (from white to black). Subsequently, the connected components of the image are extracted after the threshold. The area of each connected component is extracted and stored. At the end of the process, each of the probable regions is analyzed to determine those that remain at various values of the threshold applied previously. About the regions obtained in the previous step, you can optionally approach them with an ellipse and then keep each descriptor of the regions obtained as features.

2.2.2.9   Features from Accelerated Segment Test

The FAST algorithm was proposed by (ROSTEN; DRUMMOND, 2006) to be an algorithm to find points of interest in real-time applications.FAST is faster than the algorithms that use DoG to extract features, for example, SIFT and Harris Corner Detector because, with the use of machine learning techniques, superior performance in the use of resources and computational time is achieved.

The FAST algorithm uses a 16 pixel circle to classify whether a P point is a corner. If a N number (normally used as 12) of points inside the circle is lighter than the intensity of the point P added to a threshold or darker than the intensity of point P minus a threshold then P is classified as a corner.

To optimize the step described above, a test called "High-speed Test" was developed to reject points that are not corners analyzing only 4 pixels. Subsequently, machine learning techniques (such as decision trees) are applied to optimize the process and ensure the effectiveness of the algorithm.

CHAPTER **3**

Related works

This chapter describes the main works in multispectral registration of images obtained by UAVs, in addition to the main studies related to the proposed work.

3.1 Alignment of UAV-hyperspectral bands using keypoint descriptors in a spectrally complex environment

In this work (BANERJEE; RAVAL; CULLEN, 2018), several techniques were evaluated using descriptors of local characteristics to perform the hyperspectral registration of images in spectral complex environments, more specifically in swamps and wetlands. The authors used images of this type of environment because, according to them, performing the hyperspectral registration of this type of environment is quite complicated as it houses a wide variety of species, which leads to a wide variety of reflectance between the spectra. In this work, the authors worked with bands 515.14, 531.50, 550.14, 570.18, 610.10, 670.31, 700.08, 710.12, 720.27, 740.40, 750.19, 762.02, 780.33, 800.35 and 850.35nm.

Harris-Stephens Features (HSF), MEF, SIFT, SURF, BRISK and FAST were used to register the images. Two metrics were used to evaluate the results: RMSE and Pearson's Correlation Coefficient (PCC).

An evaluation was also carried out in this work of the best choice of target to perform the registration. The authors evaluated performing the registration in spectral order (wavelength) and in the order in which the spectra were obtained.

In the results, the authors concluded that the best order, among those evaluated, for the registration process was the spectral order. One of the main reasons that led to this result is that the spectral order minimizes the spectral difference between the images and this leads to a greater correspondence between the control points. The temporal order was unable to register and, therefore, it was considered insufficient. Among the techniques evaluated, SURF presented the best $\overline{\text{PCC}}$ and $\overline{\text{RMSE}}$.

The authors emphasize that the results can be improved using descriptors that are spectrally invariant instead of being spatially invariant (BANERJEE; RAVAL; CULLEN, 2018).

3.2   Data-driven Multispectral Image Registration

In this work (YASIR, 2018), the authors proposed the creation of an automatic framework for the registration of multispectral images. However, unlike other related works, this framework allowed intermediate targets for registration. The basic premise of the framework is the need for a minimum amount of correspondence between the control points between two channels to guarantee a low alignment error and that the greater the number of corresponding control points between the channels, the better the registration.

To obtain the control points, the authors used SIFT, BRISK, SURF and ORB techniques. The framework was evaluated by the number of control points obtained, by the computational time and by the BPE. The authors evaluated the robustness of their framework in three datasets, two with images obtained by UAVs and one obtained through a fixed platform. These datasets were chosen because they have a wide variety of different deformations.

The framework proposed by (YASIR, 2018) consists of the construction of a complete graph, where the graph nodes are the channels to be registered and the weights of the quantity control points obtained by the algorithms between these channels. Then, using the Kruskal (KRUSKAL, 1956) algorithm, a Maximum Spanning Tree (MST) is obtained. To find the channel to be used as a target for the other alignments, the MST is transformed again into a graph and the Floyd-Warshall algorithm is applied to obtain the shortest paths between all vertices (FLOYD, 1962). To accomplish that, they considered each edge with weight equals to 1. The node with the least sum of distances from itself to all other nodes is selected as the destination channel for the registration scheme. Note that there may be intermediate nodes in this process, which is one of the main advantages of this framework. A general scheme of this framework can be seen in Figure 18.

The authors compared their framework with the direct registration approach for each channel individually. In the results, it is clear the superiority of the application of this framework in obtaining control points when compared to the direct approach. However, the authors did not evaluate the registration in other orders, such as those proposed by (BANERJEE; RAVAL; CULLEN, 2018) (Temporal and Spectral), thus making their evaluation incomplete. The quality of the resulting images was also not evaluated, being analyzed only the average BPE between the channels. The authors discuss the difficulty of registering the near-IR (NIR) channel with the others, requiring intermediate registration of the NIR channel on the red-edge channel. Among the evaluated algorithms, SIFT obtained the best results, both in the number of corresponding control points and in the
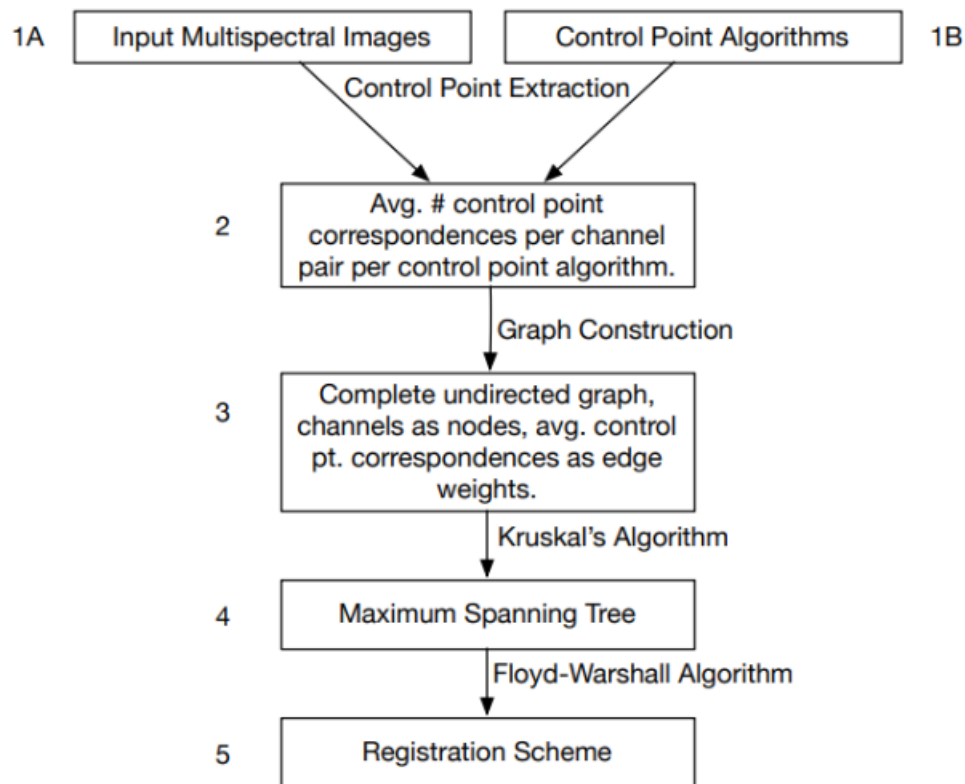
Figure 18 – Framework proposed by (YASIR, 2018).

lowest BPE (YASIR, 2018).

3.3   A Normalized SURF for Multispectral Image Matching and Band Co-Registration

The authors proposed in (JHAN; RAU, 2019) a change in the SURF method to increase its performance in registering the channels of the same image (multispectral co-registration). The authors also describe that an image obtained by a multi-lens multispectral camera has significant alignment errors and that the process of registering images between the bands is necessary. According to them, due to the non-linear intensity of spectral response, using feature-based methods for the image matching process (such as SURF) will obtain few features between the bands of the multispectral image. The images evaluated in the work were obtained from a Helicopter (MiniMCA-12) at 100 meters high and a Multi-Rotor (RedEdge Altum) at 50 meters high.

To solve this problem, a standardized version of SURF (N-SURF) was proposed, which extracts the features in only one scale, calculates the cumulative distribution function (CDF) of features, and obtains consistent features from the CDF. This method is summarized in Figure 19.

To evaluate the results, the authors used 4 metrics: 3 to measure performance when
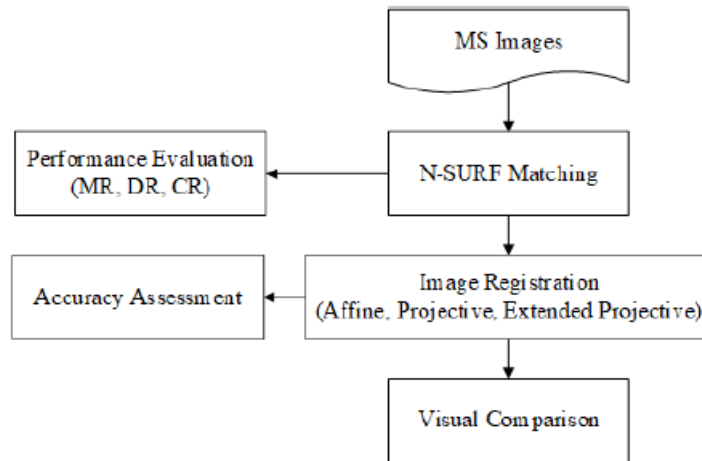
Figure 19 – Method proposed by (JHAN; RAU, 2019).

analyzing the extraction and matching of features and 1 to analyze the alignment performance at the pixel level. The metrics to assess the extraction and matching of features were: MR, that represents how many points can be matched over total features on reference and target images; DR, which computes the ratio of duplicates in matches; and CR is to calculate the percentage of correct points in none duplicate matches after rigorous image registration is conducted. To assess the alignment performance, the RMSE was used. The authors compared the SURF algorithm with its modified N-SURF proposal. The results indicated that the N-SURF was superior to the SURF in up to 3 times besides having obtained good performance in all the tested images.

The authors also proposed a change in the projective transform to correct lens and point of view distortions just once. In the evaluation between the types of transformation, it was found that among the three transformations evaluated (Affine, Projective and Extended Projective), Extended Projective obtained the best result. When combined with N-SURF, results were obtained that varied between 0.3 and 0.6 pixels of error in all the evaluated images.

3.4   Automated Coregistration of Multisensor Orthophotos Generated from Unmanned Aerial Vehicle Platforms

The authors proposed in (HAN et al., 2019) a way to perform band-by-band alignment (band co-registration) in orthophotos and not in the raw set of images obtained in flight. The authors point out that to obtain good results in the alignment process it is necessary to use GCP for georeferencing and georectification of the orthophoto. However, the cost and time limitation to assemble this apparatus on each flight causes a major inconvenience to producers.

To perform the band-to-band alignment of the orthophotos the authors propose two steps. The first step combines the coordinates between the orthophotos using the GNSS navigation data acquired during the flight for this purpose. Then, the band to be registered has its scale adjusted and is traded based on the data obtained by the GNSS to superimpose the reference image. In the second step, the phase correlation method is applied to find similarity peaks and perform another translation to obtain maximum precision. The process is summarized in Figure 20.
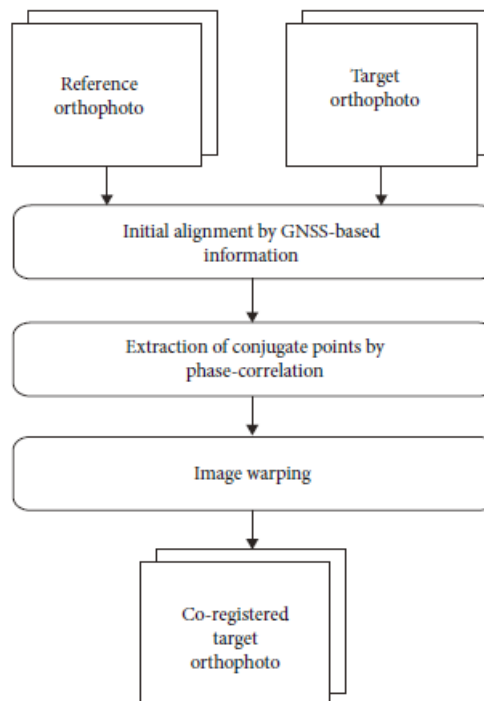
Figure 20 – Registration process proposed by (HAN et al., 2019).

To evaluate the results, the authors used two datasets (RGB-TIR and RGB-MS) obtained at an average height of 40 meters and with a spatial resolution of 1.04 cm for RGB images and 1.96 for multispectral images. The metrics used were RMSE, Correlation Coefficient (CC) and Normalized Mutual Information (NMI).

For the RGB-MS dataset, the authors obtained an average RMSE of 0.111 meters. In the RGB-TIR, the accuracy was evaluated based on the CC and the NMI, obtaining growth in the CC from 0.39 before registration to 0.41 afterward and an increase in NMI from 0.06 before registration to 0.47 afterward.

3.5   Automated Co-Registration of Multi-Temporal Series of Multi-Spectral UAV Images for Crop Monitoring

The authors in (OCHIENG'MC'OKEYO, 2018) proposed an evaluation of the registration of multispectral images obtained in the same period (intra-epoch) and in different periods (inter-epoch). The authors also conducted a discussion regarding the choice of a band to receive the alignment of the others (master-slave bands).

SURF, BRISK, MSER and KAZE methods were used for the image registration process. Tests were carried out varying the parameters of each method to optimize the methods as much as possible. The band "red-edge" was considered as the master for the alignment process. Although this band is not sensitive to vegetation, the authors justified that it is the band where most features can be obtained.

To evaluate the results obtained, the RMSE was used, and the analysis of the results showed that the SURF and KAZE methods are better for both intra-epoch and inter-epoch alignment, with SURF being the algorithm with better performance between the two.

When evaluating the standard parameters of the algorithms against the modifications proposed by the authors, it was verified that this change caused a significant improvement in the number of detected keypoints and in the amount of matching between the keypoints.

3.6   A Rigid Image Registration Based on the Non-subsampled Contourlet Transform and Genetic Algorithms

In this work (MESKINE; MILOUD; TALEB, 2010), the authors presented an algorithm for registering images using Genetic Algorithms (GA) combined with a multi-resolution framework based on the Non-Subsampled Contourlet Transform (NSCT). The genetic algorithm was adapted to minimize the search space. The approach proposed by (MESKINE; MILOUD; TALEB, 2010) uses a hybrid scheme applying the techniques of fitness sharing and elitism. Although they do not use images obtained by UAVs but by satellites, this work is very relevant to our proposal, as this work demonstrates the efficiency of bio-inspired computing techniques when applied to image registration.

Normally, a GA consists of two main components, which are dependent on the problems: chromosome coding and the evaluation function. For the problem of image registration, (MESKINE; MILOUD; TALEB, 2010) represented the chromosomes in binary form, represented by 20 bits with three genes. The R gene represents the rotation, the X

gene represents the translation on the x axis and the Y gene represents the translation on the y axis. The chromosome proposed by (MESKINE; MILOUD; TALEB, 2010) can be seen in the Figure 21. GA's search space was limited as follows: rotation was limited to ±128 degrees and translation (on the x and y axes) limited to ±32 pixels. The objective function of the GA was the correlation coefficient between the target image and the registered image.
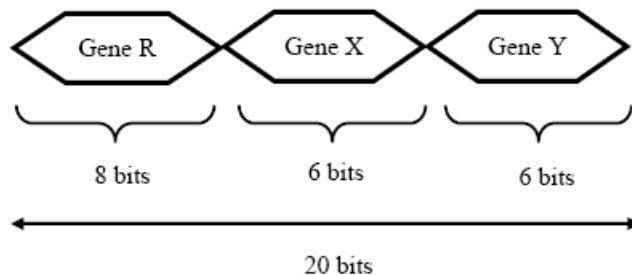
Figure 21 – Chromosome encoding proposed by (MESKINE; MILOUD; TALEB, 2010).

The basic parameters of GA were defined as follows: the population size in each generation was restricted to 80 individuals with a crossover probability of 85% and a mutation probability of 2%, and the algorithm is finalized after 100 generations. To assess the performance of the hybrid approach proposed by the authors, a first evaluation was carried out comparing hybrid GA and traditional GA. In this assessment, it was quite clear that GA with the hybrid approach considerably outperforms traditional GA.

The authors also evaluated the combination of GA and the framework based on the NSCT. To assess the quality of the registration, the RMSE was used, and according to the author's conclusion, the results were quite promising with low values of RMSE for high-resolution images obtained by satellites and radar images (MESKINE; MILOUD; TALEB, 2010).

3.7 Final considerations

Several works are proposed for the band-to-band alignment. Approaches like (BANER-JEE; RAVAL; CULLEN, 2018) and (YASIR, 2018) try to create frameworks to obtain the best order of alignment between the bands, testing for this, several methods of detection and description of features. Approaches such as (JHAN; RAU, 2019), seek to improve existing alignment methods, in this case, SURF, to make them spectrally invariant. Works like the one proposed by (HAN et al., 2019) and (OCHIENG'MC'OKEYO, 2018), perform the alignment between the mosaics obtained by each band, instead of the traditional approach of aligning image by image. Also, several works like the one proposed by (MESKINE; MILOUD; TALEB, 2010) were developed to evaluate the performance of bio-inspired methods, in this case, GA, for the alignment of multispectral images.

Unlike all the works previously proposed, which find a set of transformations to align the bands in each image, this work examines the entire dataset to find the best set of transformations to align all the images in the dataset. The risk of not aligning an image is reduced and alignment is done with as many keypoints as possible. These works are described in Table 3, where the information about the alignment order, evaluated methods, evaluated metrics and the best method obtained is detailed.

Table 3 – Summary of works in the literature for the band-to-band alignment of multispectral and hyperspectral images.

Reference	Alignment Order	Evaluated methods	Evaluation Metrics	Best Method
(BANERJEE; RAVAL; CULLEN, 2018)	Spectral and Temporal	HSF, MEF, SIFT, SURF, BRISK and FAST	RMSE and PCC	SURF
(YASIR, 2018)	Variable according to dataset	SIFT, BRISK, SURF and ORB	BPE	SIFT
(JHAN; RAU, 2019)	Blue as Reference	SURF and N-SURF	MR, DR, CR and RMSE	N-SURF
(HAN et al., 2019)	RedEdge as Reference	SURF, BRISK, MSER and KAZE	RMSE	SURF
(MESKINE; MILOUD; TALEB, 2010)	-	GA	RMSE	GA

Methodology

4.1 Datasets

In our experiments we used two datasets to evaluate the proposal performance, both containing images with 1280×960 pixels size and an average of 80% overlap between images. The spectra present in the images are, blue (475nm center, 20nm bandwidth), green (560nm center, 20nm bandwidth), red (668nm center, 10nm bandwidth), red edge (red-edge) (717nm center, 10nm bandwidth), near-IR (nir) (840nm center, 40nm bandwidth). Images were obtained on a single flight without any kind of pre-processing and using a MicaSense Red-Edge camera (MicaSense Inc. Seattle, WA, USA) coupled to a Micro UAV SX2 (see Figure 22) (Sensix Innovations in Drone Ltda, Uberlândia, MG, Brazil) at an average height of 100 meters and an average speed of 20 m/s. At this altitude, the ground sample distance (GSD) is 6.8 cm/pixel.

Figure 22 – Micro UAV SX2 by Sensix.

The first dataset was obtained from a soybean plantation located at the following decimal coordinate $(-17.877308292165985, -51.08216452139867)$. This dataset contains 1080 images (216 scenes and 5 channels), as shown in Figure 23.

The second dataset was obtained from a cotton plantation at the following decimal coordinate $(-17.820275501545474, -50.32411830846922)$ and it contains 830 images (166 scenes and 5 channels), as shown in Figure 24.
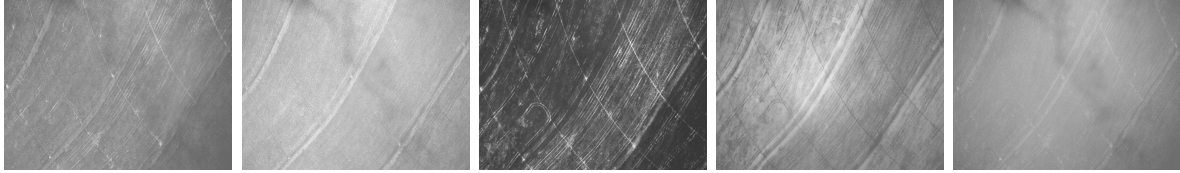
Figure 23 – Example of an image scene containing all channels (Blue, Green, Red, near-IR, red-edge respectively) of the soybean plantation dataset.
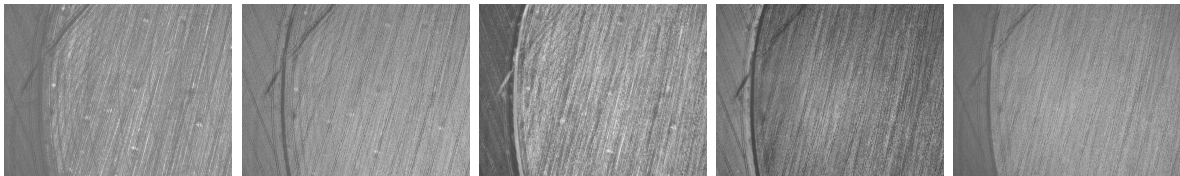
Figure 24 – Example of an image scene containing all channels (Blue, Green, Red, near-IR, red-edge respectively) of the cotton plantation dataset.

To measure the performance of the alignment process between the bands present in the datasets, each dataset was sent to a specialist so that he performed the manual marking of 12 points on the green band and subsequently scored the equivalent points on the other bands (red, blue, near-IR and red-edge).

4.2   UAV-Multispectral sensed data band co-registration framework

The proposed UAV-Multispectral sensed data band co-registration framework aims to align the bands of multispectral images obtained by UAVs using feature-based methods for this purpose. Unlike the various band co-registration approaches that perform a different alignment process for each scene (i.e., set of bands), our method seeks the best transformation set among all the dataset images to later align all the scenes using the same transformation set.

This approach receives as input a multispectral image dataset and, as output, it returns a schema, i.e., order in which bands should be aligned and which transformation should be used in each alignment. Note that, unlike the frameworks proposed in the chapter 3, which try to perform an alignment in each scene, the chance of failure of our method is drastically reduced because it will always search the dataset for the best set of transformations to align the bands. Each step of the proposed framework will be explained in the following sections.

4.2.1 Keypoint extraction and graph construction

For each multispectral scene, we combine the bands two at time. For each combination, the number of keypoints, after the elimination of outliers, is extracted by each method given as input into the framework. The number of keypoints, the image identifier, the feature extraction method that generated these keypoints, and the band combination, is stored in a tuple.

Given the set of tuples extracted previously, for each band combination, the tuple that returns the largest number of keypoints is obtained. Note that for a dataset that contains 5 bands (*red*, *green*, *blue*, *nir*, *rededge*) in each scene, at the end of this step 10 maximum tuples will be obtained: $red - green$, $red - blue$, $red - nir$, $red - rededge$, $green - blue$, $green - nir$, $green - rededge$, $blue - nir$, $blue - rededge$, $nir - rededge$. - At the end of this step, a complete undirected weighted graph G is constructed, with the bands as nodes and the maximum tuples, i.e., tuples that obtained the most keypoints, as edges. Each edge is labeled with the image, technique that generated that edge and the number of keypoints. The edge weights are represented by the number of keypoints obtained. Figure 25 demonstrates the output of this step.

4.2.2 Schema construction

With the graph G obtained in the previous step, some graph algorithms are applied to transform the complete graph into a schema that will represent the best order to perform the multispectral alignment. Starting from the graph G, we applied the Kruskal (KRUSKAL, 1956) algorithm to construct a Maximum Spanning Tree (MST). To find the channel to target for alignments, the weights between the nodes are replaced by 1 and the Floyd-Warshall all-pairs-shortest-path (FLOYD, 1962) algorithm is used. The node with the smallest sum of distances from itself to all the other nodes is selected as the target channel for the registration schema. Subsequently, each undirected edge (a, b) is converted to a directed edge (a, b) if b is closer to the target channel, otherwise (b, a). Figure 26 shows the output for this step, this figure represents the order in which the bands should be aligned. First, align the blue and nir with the green and then align the red with the blue and the rededge with the nir.

4.2.3 Construction of transformations and dataset alignment

At the end of the previous process, we have a directed G_{schema} graph that represents the best order to perform the alignment process. Note that through this method it is possible to have intermediate alignments, to guarantee a better alignment among the channels. As can be seen in Figure 26, each edge of this graph belongs to a method and an image present in the dataset whose combination presents the largest number of keypoints for two bands (which, in this case, it will be the nodes that this edge connects).
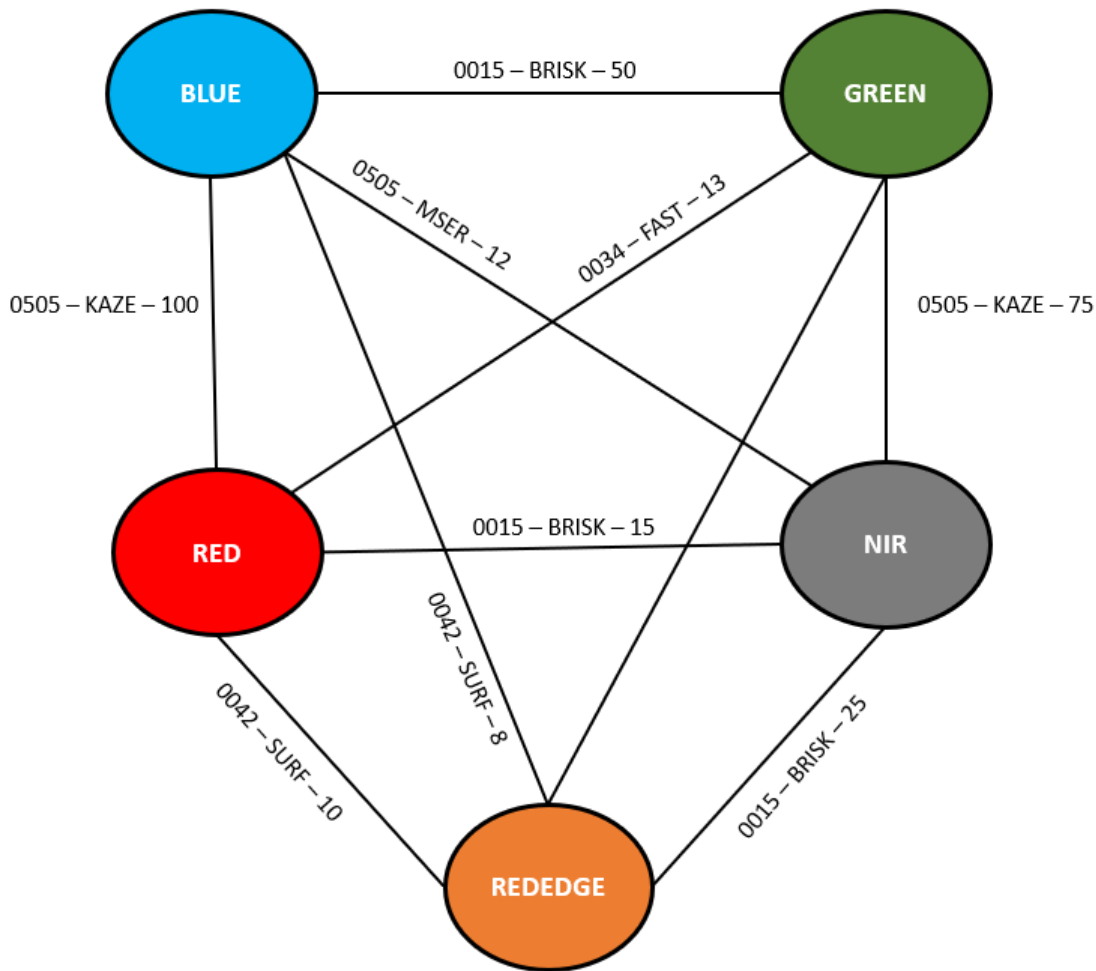
Figure 25 – Complete undirected weighted graph G. The edges is labeled, respectively, with image id, method and the number of keypoints.

For each of the edge present in G_{schema}, the transformation function is extracted to align one node with the other.

Note that when extracting all the transformations, we can perform the alignment process among the bands in an optimal way, that is, with the best transformation, considering the number of keypoints obtained, that could be estimated in the dataset. With the transformations obtained, all the scenes present in the dataset are aligned using this same set of transformations.

4.3   Evaluation methodology

As inputs to the framework we used the following keypoints extraction methods: BRISK, FAST, MSER, HARRIS, SURF and KAZE. The choice of these methods was based on the bibliographic review presented in the chapter 3, all of them were used in several works obtaining satisfactory results in the process of multispectral alignment of images obtained by UAVs.
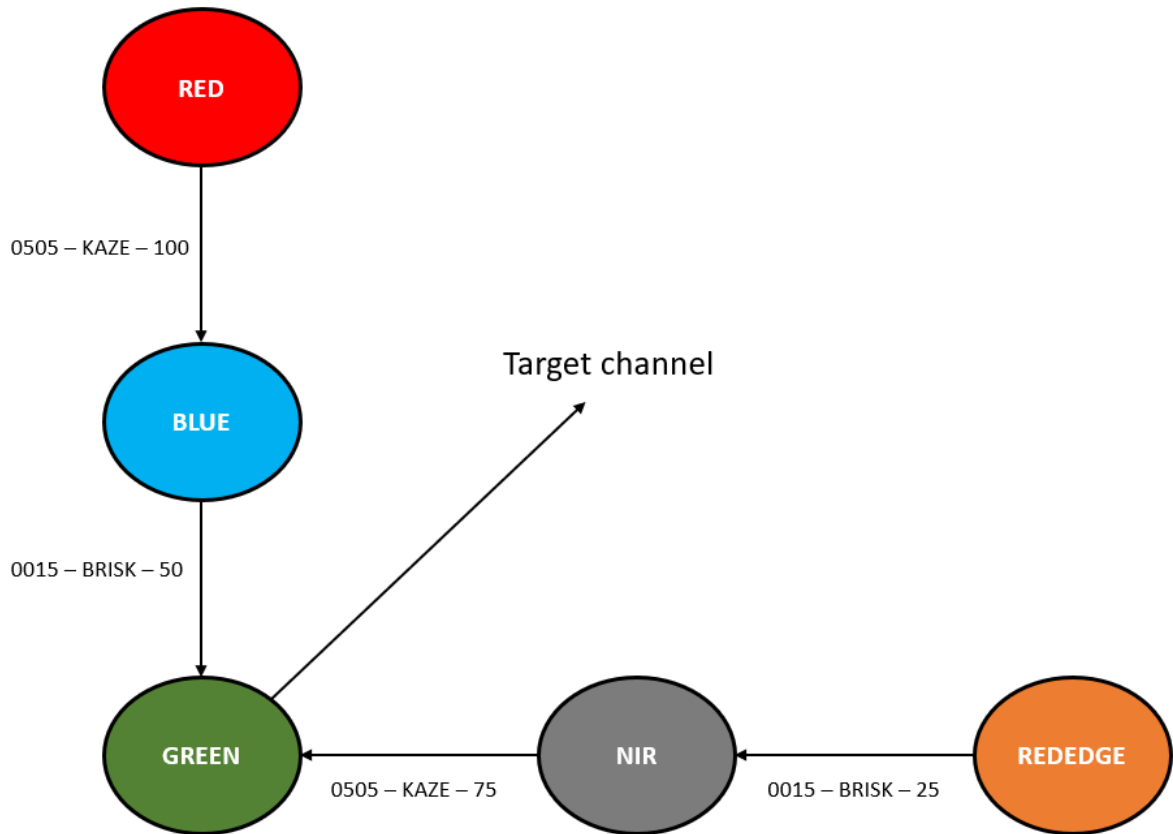
Figure 26 – Final registration Schema

To evaluate the performance of our approach, we compared it with the frameworks presented in Sections 3.1 and 3.2, as these have demonstrated good results for automatically aligning multispectral images obtained by UAVs.

The metric used to validate the approach proposed by this work was the BPE. BPE has been widely used to determine the quality of image alignment in general, and this metric is used in several works presented in Chapter 3.

CHAPTER **5**

Experimental Results

5.1 Natural Misalignment

As explained in section 2.1.3.3, multispectral cameras usually use different sensors for the acquisition of each channel. This physical displacement between the sensors causes a misalignment between the resulting images. Figure 27 exemplifies this misalignment.
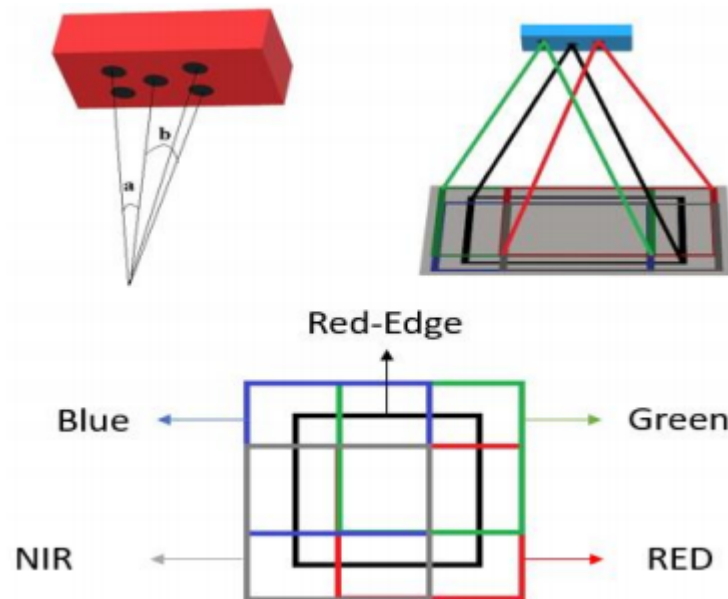
Figure 27 – Natural misalignment among sensors, from (HASSANPOUR; JAVAN; AZIZI, 2019).

Tables 4 and 5 show the average misalignment between the ground-truth and the images present in each dataset. We can observe that, for the cotton dataset, the misalignment is slightly higher than that presented in soybean. This difference in misalignment between the datasets can be explained by variations between the sensors of the cameras used during the acquisition and also by variations in the acquisition altitude.

It is also important to note that the capture process between the bands is done in a synchronized way for most multispectral cameras on the market. In a worse case, i.e.,

Table 4 – Average of misalignment, in pixels, between the sensors present in the soybean
dataset.

	Blue	Green	Red	Nir	Rededge
Blue	-	5.18	15.75	15.07	12.14
Green	5.18	-	15.09	12.33	4.02
Red	15.75	15.09	-	29.25	14.79
Nir	15.07	12.33	29.25	-	16.17
Rededge	12.14	4.02	14.79	16.17	-

Table 5 – Average of misalignment, in pixels, between the sensors present in the cotton
dataset.

	Blue	Green	Red	Nir	Rededge
Blue	-	28.30	12.11	33.28	8.48
Green	28.30	-	21.44	24.01	35.66
Red	12.11	21.44	-	14.94	21.30
Nir	33.28	24.01	14.94	-	39.37
Rededge	8.48	35.66	21.30	39.37	-

where the acquisition process between the sensors was sequential, we could estimate the
misalignment between the first and the last capture.

Basically, for a common multispectral camera, the maximum recommended exposure
time is 2.5 ms and the recommended speed of a UAV, for the acquisition process, varies
between 5 and $25m/s$. Analyzing the worst case, we have that the time between the
first and the last acquisition is $10ms$, which at $25m/s$, will generate a displacement
of $25cm$. Result that for the camera used in this work at 100 meters high, it would
be a displacement of 3.67 pixels. However, the scenario above is unreal since, for the
vast majority of multispectral cameras that are used in PA, the acquisition process is
synchronized between all sensors.

5.2   Registration Schema

Each framework analyzed in this work is based on the construction of a schema, i.e.,
a band order for the band co-registration process. It is observed that the spectral schema
proposed by (BANERJEE; RAVAL; CULLEN, 2018) is independent of the dataset, while
the framework proposed by (YASIR, 2018) and our approach are oriented by dataset.
Figure 28 the schema proposed by (BANERJEE; RAVAL; CULLEN, 2018).

5.3   Soybean dataset

As described in Section 4.1, the soybean dataset presents a total of 1080 images
(216 scenes and 5 bands). We used each feature extraction method as an input for
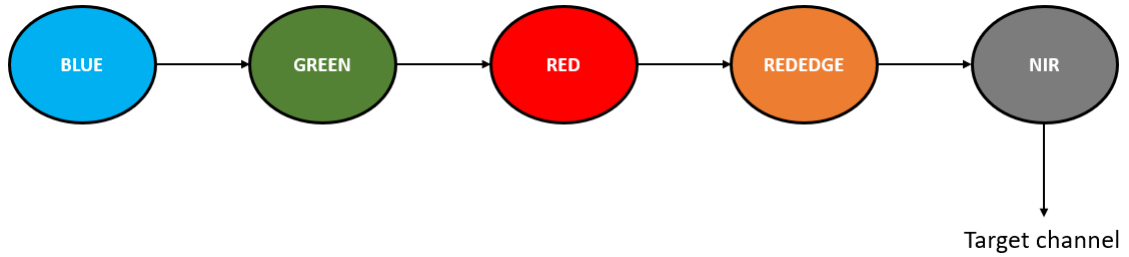
Figure 28 – Band-to-band registration schema proposed by (BANERJEE; RAVAL; CULLEN, 2018). The arrows represent the order of alignment, in this case, rededge on nir, red on rededge, green on red and finally blue on green.

the frameworks. Figures 29 and 30 show the result, respectively, of our approach and the approach proposed by (YASIR, 2018).
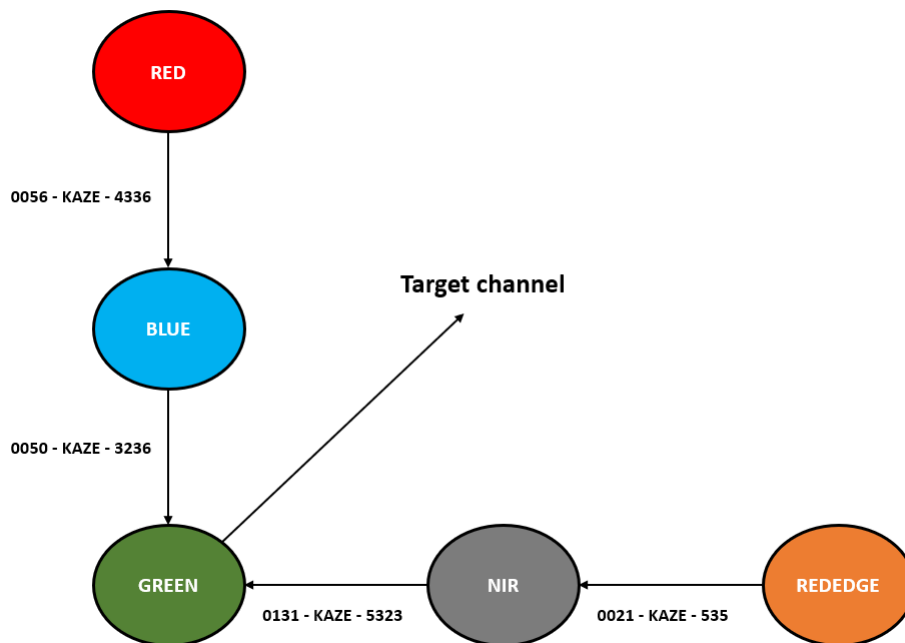
Figure 29 – Scheme generated by our approach for the soybean dataset. The caption for each edge consists of: Image ID - Method - Number of Keypoints.

Note that, despite generating the same schemes, our approach obtained a greater number of keypoints per band than the framework proposed by (YASIR, 2018). It is also important to note that each alignment will be made using a different image, obeying the premise of maximizing the number of keypoints for the best band-to-band alignment.

Table 6 shows the accuracy of each method, i.e., the number of alignments the method was able to perform. Note that, since the soybean dataset has 1080 images, each method should have performed a total of 864 alignments (for 5 bands, 4 alignments are required). It is also important to note that the framework proposed by (BANERJEE; RAVAL; CULLEN, 2018) deals individually with each feature extraction method.

As can be seen in Table 6, by using a global transformation in all images, our approach was able to perform all alignments. The framework proposed by (YASIR, 2018) and the
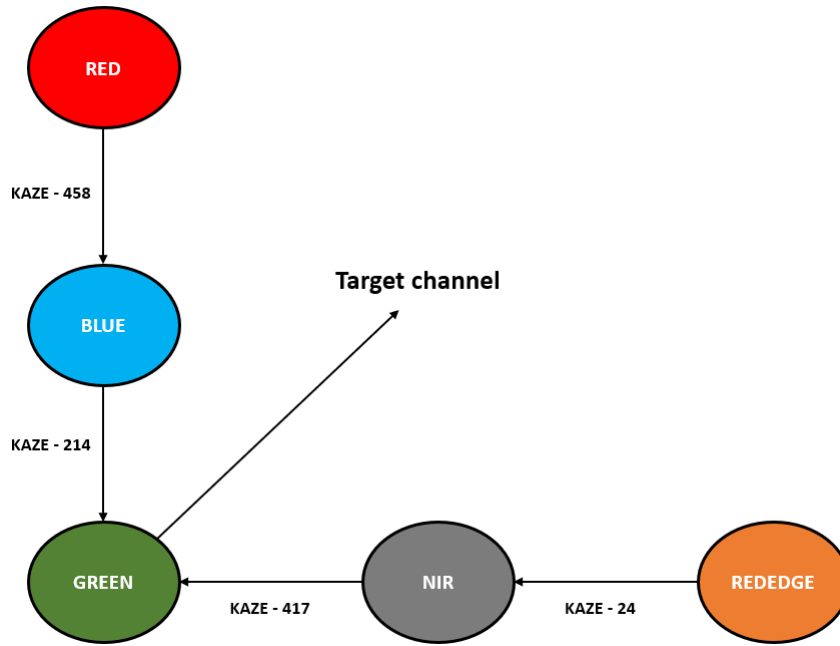
Figure 30 – Scheme generated by the approach proposed in (YASIR, 2018) for the soy-
bean dataset. The caption for each edge consists of: Method - Number of
Keypoints.

Table 6 – The accuracy obtained by the frameworks in the alignment of the soybean
dataset.

Method	Failures	Accuracy
Our approach	0	100.00%
(YASIR, 2018)	183	78.82%
(BANERJEE; RAVAL; CULLEN, 2018) KAZE	352	59.26%
(BANERJEE; RAVAL; CULLEN, 2018) HARRIS	673	22.11%
(BANERJEE; RAVAL; CULLEN, 2018) SURF	677	21.64%
(BANERJEE; RAVAL; CULLEN, 2018) MSER	802	7.18%
(BANERJEE; RAVAL; CULLEN, 2018) BRISK	830	3.94%
(BANERJEE; RAVAL; CULLEN, 2018) FAST	842	2.55%

approach proposed by (BANERJEE; RAVAL; CULLEN, 2018) with the KAZE method
were the only ones that managed to achieve more than 50% of accuracy in the alignment.
All methods that failed to achieve a minimum of 50% alignment were considered inept
and discarded from comparing alignment quality.

Table 7 shows the BPE obtained by each framework. Note that our approach obtained
an average BPE close to 0 (0.146 pixels). The approach proposed by (YASIR, 2018) also
obtained a good result when compared to the framework proposed by (BANERJEE;
RAVAL; CULLEN, 2018) in conjunction with the KAZE method.

Regardless of the framework used for the soybean dataset, the best method for extract-
ing control points for band-to-band alignment in aerial images was the KAZE features
proposed by (ALCANTARILLA; BARTOLI; DAVISON, 2012).

Table 7 – Registration performance evaluation on Soybean dataset.

Method	BPE
Our approach	0.14
(YASIR, 2018)	1.33
(BANERJEE; RAVAL; CULLEN, 2018) KAZE	40.50

Figures 31, 32 and 33 show the worst alignment obtained by our approach in the soybean dataset. It is possible to observe in the figures that the performance, even in the worst case, was extremely satisfactory, generating no visible anomaly in the figures.
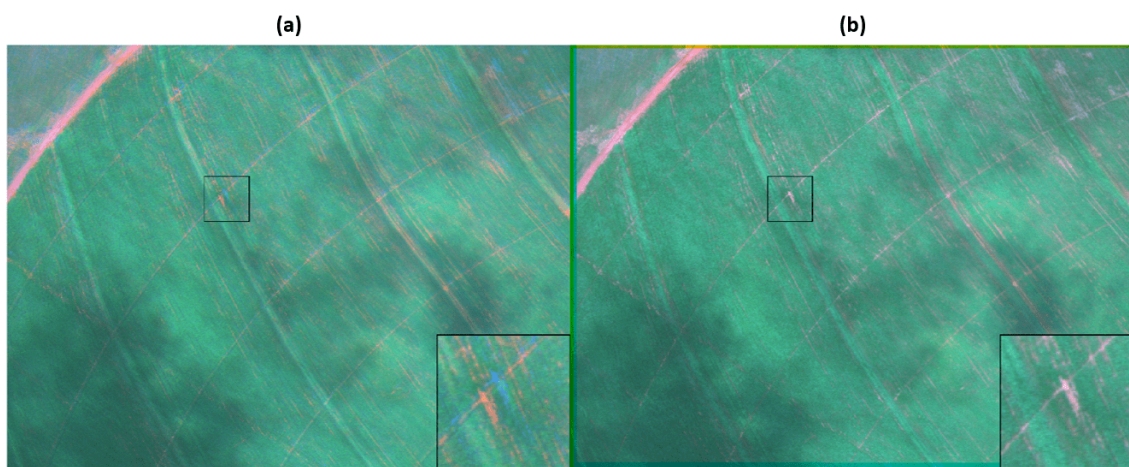
Figure 31 – Worst alignment achieved by our approach in the Soybean dataset. (a) It is the original RGB image; (b) It is the aligned RGB image.
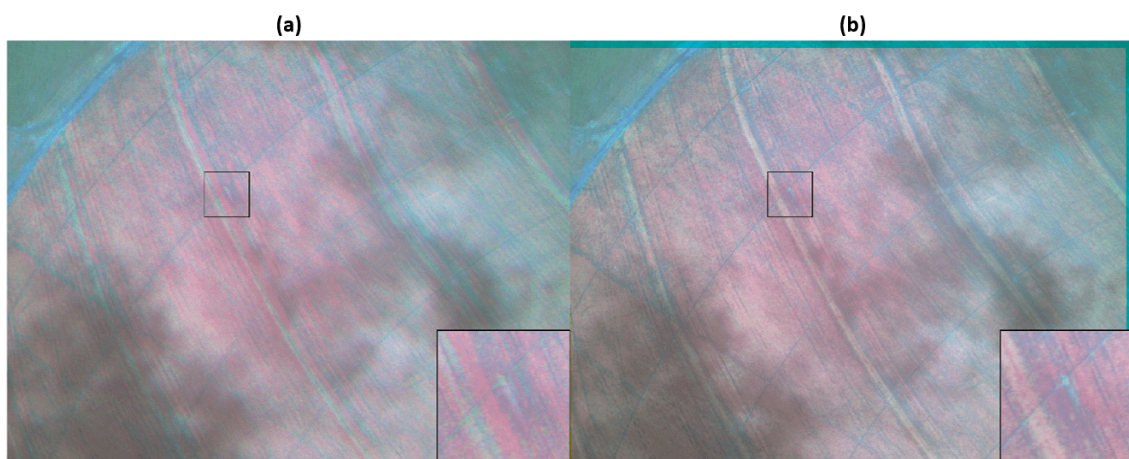
Figure 32 – Worst alignment achieved by our approach in the Soybean dataset. (a) It is the RGB image (with the red (R) channel replaced by the rededge and the blue (B) channel replaced by the nir); (b) It is the aligned RGB image (with the red channel (R) replaced by rededge and the blue channel (B) replaced by nir).
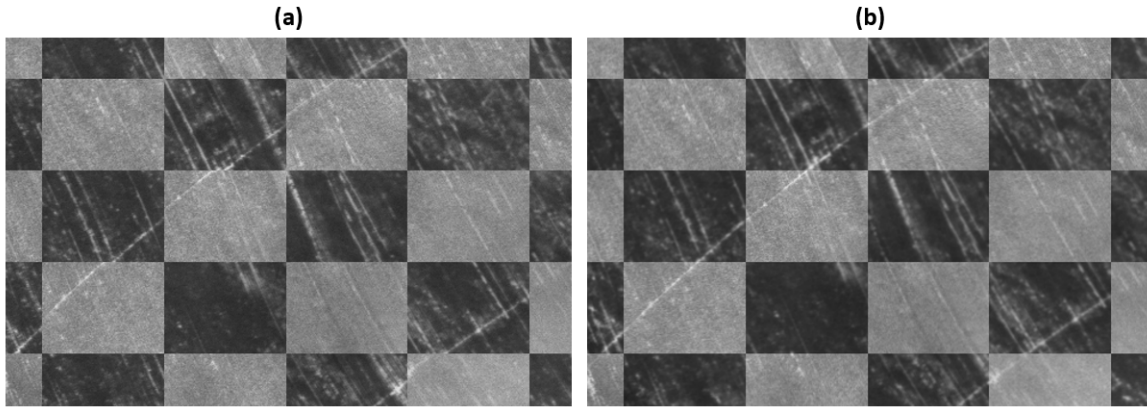
Figure 33 – Worst alignment achieved by our approach in the Soybean dataset. (a) It is the checkerboard between original blue and red bands; (b) It is the checkerboard between aligned blue and red bands.

5.4   Cotton dataset

As described in Section 4.1, the cotton dataset presents a total of 830 images (166 scenes and 5 bands). The methodology for evaluation was the same used in the soybean dataset, i.e., we used each feature extraction method as an input for the frameworks. Figures 34 and 35 show the result schema, respectively, of our approach and the approach proposed by (YASIR, 2018).
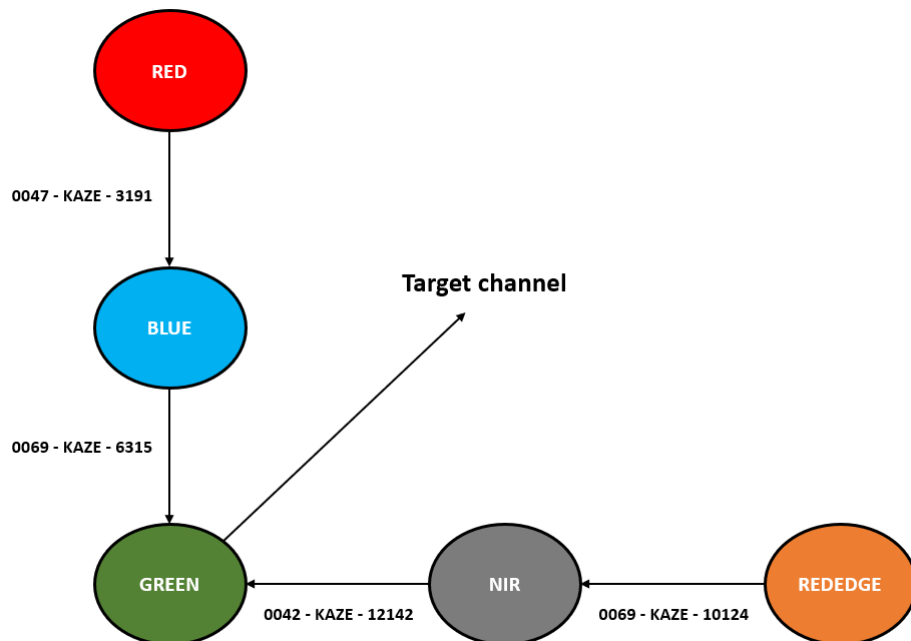
Figure 34 – Scheme generated by our approach for the cotton dataset. The caption for each edge consists of: Image ID - Method - Number of Keypoints.

As in the soybean dataset, we can see that the number of keypoints obtained by our approach to align the bands is higher when compared to the approach proposed by
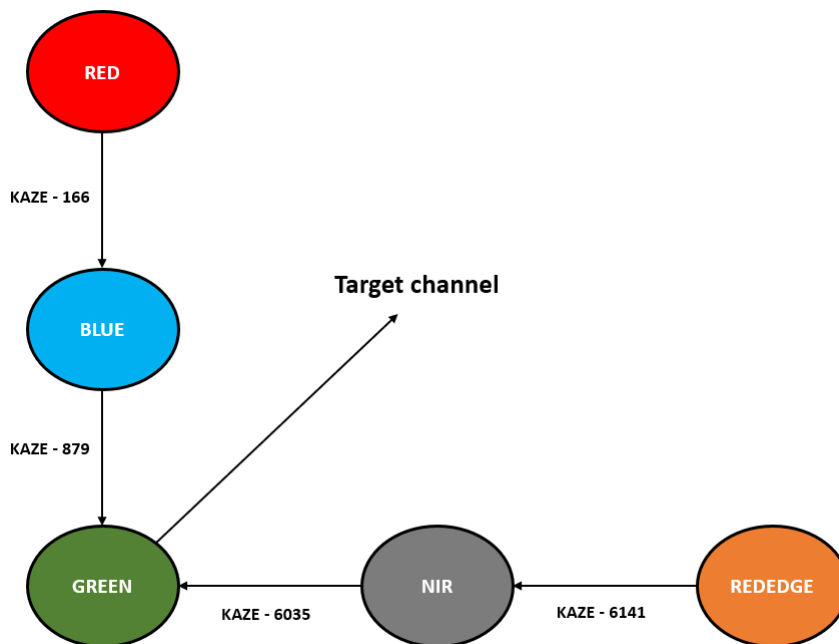
Figure 35 – Scheme generated by the approach proposed in (YASIR, 2018) for the cotton dataset. The caption for each edge consists of: Method - Number of Keypoints.

(YASIR, 2018). Again, we can see that the feature extraction method that managed to obtain more control points was KAZE.

Subsequently, the accuracy of each method was assessed for the dataset and the results are shown in Table 8. Note that, unlike the soybean dataset, for the cotton dataset the methods obtained greater accuracy. Our approach, using a global transformation, managed to align all the images. The approach proposed by (YASIR, 2018) also achieved good results with only 1 alignment out of the 664 possible. The framework proposed by (BANERJEE; RAVAL; CULLEN, 2018) was also able to achieve accuracy greater than 50% in three feature extraction method: MSER, SURF and KAZE.

Table 8 – The accuracy obtained by the frameworks in the alignment of the cotton dataset.

Method	Failures	Accuracy
Our approach	0	100.00%
(YASIR, 2018)	1	99.85%
(BANERJEE; RAVAL; CULLEN, 2018) KAZE	165	75.15%
(BANERJEE; RAVAL; CULLEN, 2018) SURF	200	69.88%
(BANERJEE; RAVAL; CULLEN, 2018) MSER	240	63.86%
(BANERJEE; RAVAL; CULLEN, 2018) HARRIS	382	42.47%
(BANERJEE; RAVAL; CULLEN, 2018) FAST	390	41.27%
(BANERJEE; RAVAL; CULLEN, 2018) BRISK	431	35.09%

Table 9 shows the BPE obtained by each framework. Our approach obtained an average BPE of 0.71 pixels. Despite being a result inferior to that obtained in the soybean

dataset, our approach still obtained the best result when compared to the proposed by (YASIR, 2018) and (BANERJEE; RAVAL; CULLEN, 2018). The framework proposed by (BANERJEE; RAVAL; CULLEN, 2018) obtained a low performance, regardless of the method for extracting features.

Table 9 – Registration performance evaluation on Cotton dataset.

Method	BPE
Our approach	0.71
(YASIR, 2018)	1.54
(BANERJEE; RAVAL; CULLEN, 2018) KAZE	31.19
(BANERJEE; RAVAL; CULLEN, 2018) SURF	84.97
(BANERJEE; RAVAL; CULLEN, 2018) MSER	132.60

As with the soybean dataset, the best method for extracting control points for band-to-band alignment in aerial images was the KAZE features proposed by (ALCANTARILLA; BARTOLI; DAVISON, 2012).

Figures 36, 37 and 38, show the worst alignment obtained by our approach in the cotton dataset. We can see that the cotton dataset has noise throughout the image. However, even with the noise, the alignment result was also satisfactory for the worst case, with no anomalies or misaligned stretches.
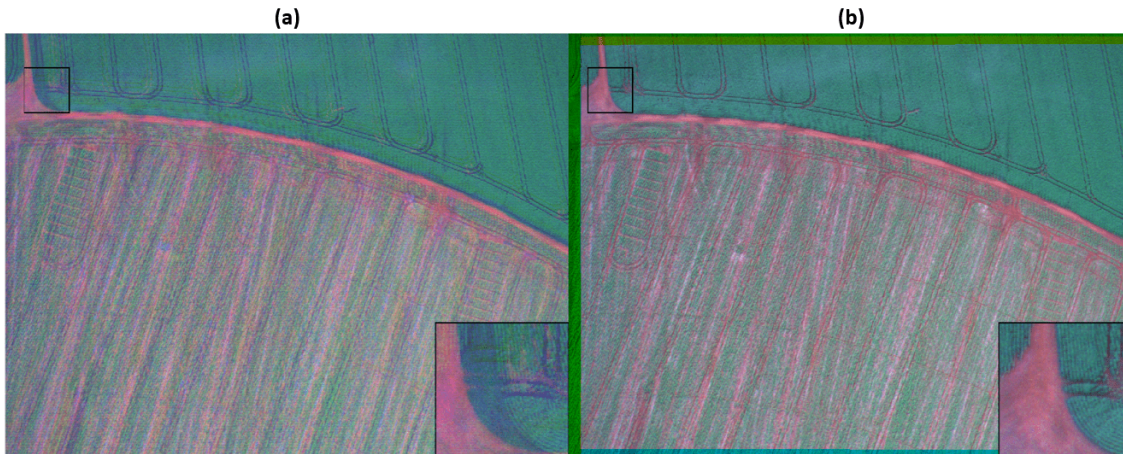
Figure 36 – Worst alignment achieved by our approach in the Cotton dataset. (a) It is the original RGB image; (b) It is the aligned RGB image.

5.5 Execution Time of the Framework

Subsequently, we compare the execution time of our approach with the other evaluated frameworks. To accomplish that, each framework was executed twice in a single thread and the average execution time was computed. As previously stated, our framework computes the best multispectral band co-registration schema for each dataset. Table 10
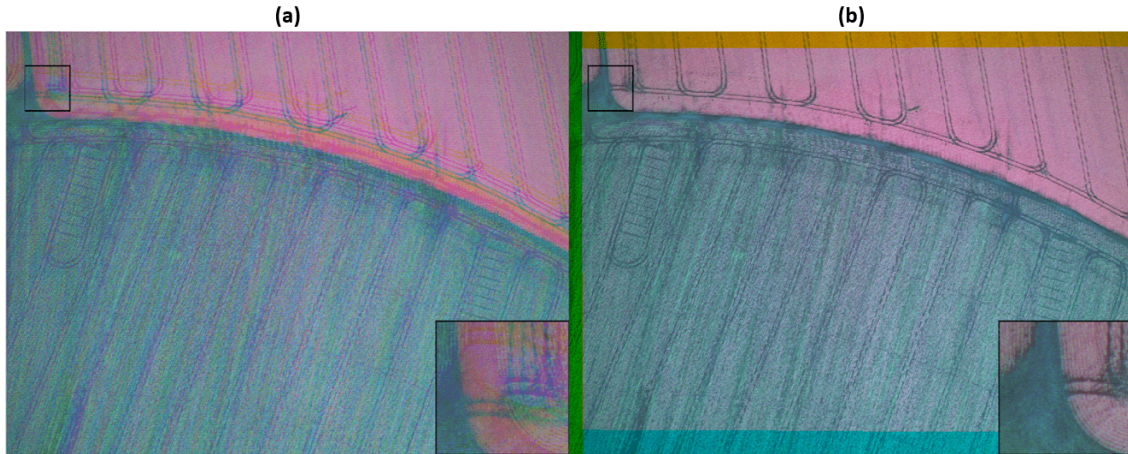
Figure 37 – Worst alignment achieved by our approach in the Cotton dataset. (a) It is the RGB image (with the red (R) channel replaced by the rededge and the blue (B) channel replaced by the nir); (b) It is the aligned RGB image (with the red channel (R) replaced by rededge and the blue channel (B) replaced by nir).
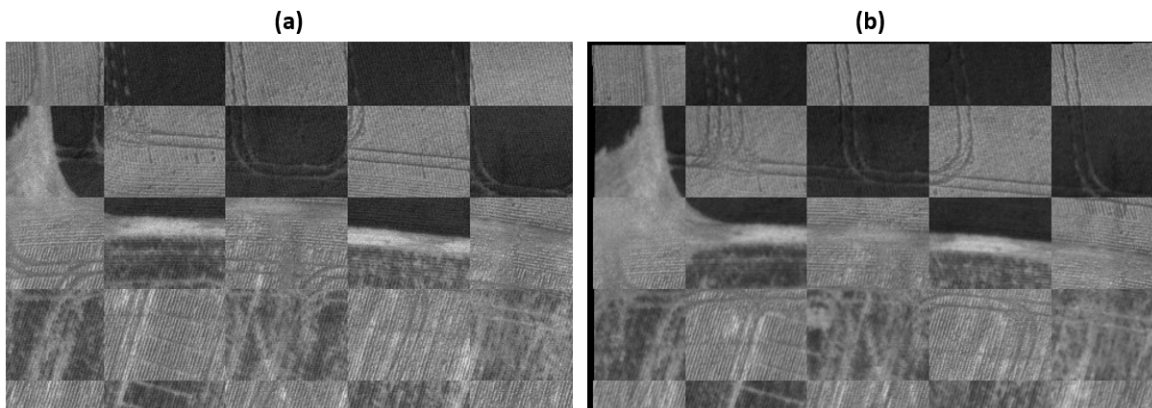
Figure 38 – Worst alignment achieved by our approach in the Cotton dataset. (a) It is the checkerboard between original blue and red bands; (b) It is the checkerboard between aligned blue and red bands.

presents the average running time of the frameworks, in seconds, for both Soybean and Cotton datasets.

Table 10 – Average execution time obtained by frameworks in the datasets.

Dataset	Framework	Execution Time (s)
Soybean	(BANERJEE; RAVAL; CULLEN, 2018) KAZE	1235
	Our Approach	8808
	(YASIR, 2018)	10162
Cotton	(BANERJEE; RAVAL; CULLEN, 2018) KAZE	2145
	Our Approach	16339
	(YASIR, 2018)	18550

It is possible to notice that the execution time is extremely dependent on the data

that is being processed, for example, the soybean dataset, despite having more images, has a lower execution time. This fact is mainly due to the number of features that each method extracted from the images, the greater the number of features, the longer the time for feature matching and the transformation estimation.

The approach proposed by (BANERJEE; RAVAL; CULLEN, 2018) obtained a lower execution time because, in addition to evaluating only one technique (KAZE), it does not perform any type of analysis of the best way to perform the alignment. The approach proposed by (YASIR, 2018) had a worse result than the one proposed in this work because, after evaluating the dataset for the schema construction, it still estimates for each image the transformation function, which results in the worst execution time evaluated.

Despite the considerable execution time, our method can be parallelized in as many threads as needed, which will dramatically decrease the execution time.

5.6   KAZE superiority

As seen in the results for the soybean and cotton datasets, the best method for feature extraction, independent of the evaluated framework, was KAZE. As already explained in Section 2.2.2.6, KAZE, unlike methods such as SIFT and SURF, detect and describes features in a non-linear scale-space using non-linear diffusion filtering. For this reason, the blurring process is locally adaptable in the image, which reduces noise while maintaining the natural boundaries of objects, thus achieving superior accuracy and location distinction. In the work (ANDERSSON; MARQUEZ, 2016), a comparative study was carried out with several methods of resource extraction and detection, and, as described by the authors, KAZE performed well when analyzing a change in lighting.

It is important to note that aerial images of plantations obtained by UAVs usually present few details useful for the alignment process. Most of these details are borders, i.e., transitions from soil to plant and vice-versa, due to the difference in reflection from soil to a plant, as we can see in Figure 39.

Given these facts, KAZE is an extremely useful detector and descriptor for dealing with edges. Its proposal to create a non-linear scale space, makes the edges of the reflection transitions more detectable and distinguishable, thus obtaining a superior result among other techniques.

5.7   Framework and experiments limitations

The main limitation of this framework is the fact that it is camera oriented. This implies that to be executed, the dataset informed must have been obtained by the same camera and, preferably, on the same flight. This limitation comes from the basic premise of this framework, which is to align the sensors of the same camera, not being possible to
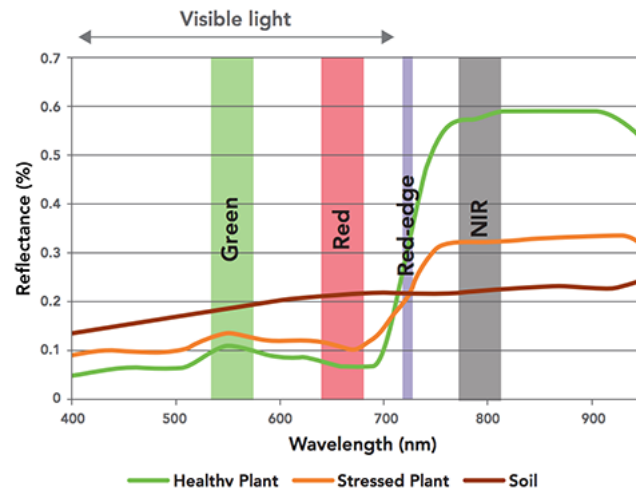
Figure 39 – The reflectance curve of a typical plant, from (FASTIE; JOGNSON; MC-
COLLAM, 2018).

use them to align bands obtained for different cameras. Note that the alignment between
the scenes is not being addressed in this work, i.e., this framework was developed to
perform the band co-registration.

Another major limitation in our work is the fact that, due to the high cost of acquisition
of multispectral cameras, we do not test other cameras to check if the framework is robust
to the main multispectral cameras on the market. Another important point is that all
the datasets evaluated were obtained by a fixed-wing. Therefore, we cannot say whether
the framework is also robust to multi-rotors.

CHAPTER **6**

Conclusion

This work presented a new method to perform the band co-registration of multispectral images obtained by UAV. Unlike the other methods, which seek to perform an alignment for each scene, our approach assumes that the speed of the UAV, when compared to the speed of image acquisition between sensors, is not sufficient to cause distortions beyond the natural ones caused by the distance between the sensors. For this reason, our approach searches among the whole dataset, the best group of images to align each band and then build an alignment schema, i.e., the order in which the bands will be aligned. Our approach was compared to two other frameworks for band co-registration in the literature.

As presented in Section 5, our approach was, on average, 335% better than the second-best framework, obtaining for the soybean dataset an alignment with a BPE close to zero (0.14 pixels) and for the cotton dataset a BPE of 0.71 pixels. The BPE of the cotton dataset was caused mainly by images with a lot of noise, as shown in section 5.4. This fact shows that a study on noise smoothing methods is necessary to obtain better results.

In Tables 6 and 8 the main problem of methods that try to carry out a different alignment for each band was demonstrated. Most of the time, for some images, it is not possible to find enough keypoints to estimate a transformation function, which makes it impossible to align the image. Our approach uses a global transformation and, for this reason, manages to carry out all the alignments.

The results obtained were relevant and show that the framework presented in this work can be used to align the bands of multispectral images obtained by UAV.

6.1   Main contributions

The main contribution of this work is the proposed framework for the process of band co-registration in images obtained by UAV. This method presents a new approach for the band-to-band alignment and obtained a superior result to the evaluated frameworks.

The second contribution is the creation of two multispectral image datasets obtained by UAVs properly aligned by an expert to measure the performance of methods for the

band co-registration process.

6.2   Future Work

The results obtained by this work demonstrate the good performance obtained by the proposed framework and motivate new lines of investigation, such as: Evaluation of datasets obtained by different multispectral cameras; Evaluation of datasets obtained by multi-rotors aircraft; Evaluation of methods to be included in the framework as pre-processing (e.g., enhancement and smoothing).

6.3   Contributions in Bibliographic Production

❏ DIAS JUNIOR, J. D.; BACKES, A. R. ; ABDALA, D. ; ESCARPINATI, Maurício Cunha. Assessing the adequability of image feature descriptors on registration of UAV-multispectral sensed data. In: XIV Workshop de visão computacional, 2018, Ilhéus. Anais do 14º Workshop de Visão Computacional, 2018. p. 56-60.

❏ Dias Jr., J. D.; Backes, A. and Escarpinati, M. C. (2019). Detection of Control Points for UAV-Multispectral Sensed Data Registration through the Combining of Feature Descriptors. In Proceedings of the 14th International Joint Conference on Computer Vision, Imaging and Computer Graphics Theory and Applications - Volume 4: VISAPP, ISBN 978-989-758-354-4, pages 444-451. DOI: 10.5220/0007580204440451

❏ Dias Jr., J. D.; Backes, A.; Escarpinati, M. C; Silva, L. H. F. P.; Costa, B. C. S. and Avelar, M. H. F. (2020). Assessing the Adequability of FFT-based methods on Registration of UAV-Multispectral Images. In Proceedings of the 15th International Joint Conference on Computer Vision, Imaging and Computer Graphics Theory and Applications. (Accepted for publication)

Bibliography

AGRICULTURA, P. e. A. Ministério da. **Agropecuária Brasileira em Números**. 2019. Disponível em: <http://www.agricultura.gov.br/assuntos/politica-agricola/agropecuaria-brasileira-em-numeros>.

ALCANTARILLA, P. F.; BARTOLI, A.; DAVISON, A. J. Kaze features. In: FITZGIBBON, A. et al. (Ed.). **Computer Vision − ECCV 2012**. Berlin, Heidelberg: Springer Berlin Heidelberg, 2012. p. 214–227. ISBN 978-3-642-33783-3.

ANDERSSON, O.; MARQUEZ, S. R. **A comparison of object detection algorithms using unmanipulated testing images: Comparing SIFT, KAZE, AKAZE and ORB**. Dissertação (Mestrado), 2016.

BANERJEE, B. P.; RAVAL, S. A.; CULLEN, P. J. Alignment of uav-hyperspectral bands using keypoint descriptors in a spectrally complex environment. **Remote Sensing Letters**, Taylor & Francis, v. 9, n. 6, p. 524–533, 2018. Disponível em: <https://doi.org/10.1080/2150704X.2018.1446564>.

BAY, H.; TUYTELAARS, T.; GOOL, L. V. Surf: Speeded up robust features. In: LEONARDIS, A.; BISCHOF, H.; PINZ, A. (Ed.). **Computer Vision − ECCV 2006**. Berlin, Heidelberg: Springer Berlin Heidelberg, 2006. p. 404–417. ISBN 978-3-540-33833-8.

BERNI, J. A. J. et al. Thermal and narrowband multispectral remote sensing for vegetation monitoring from an unmanned aerial vehicle. **IEEE Transactions on Geoscience and Remote Sensing**, v. 47, n. 3, p. 722–738, March 2009. ISSN 0196-2892.

DRONEDEPLOY. **Choosing the Right Mapping Drone for Your Business Part I: Multi-Rotor vs. Fixed Wing Aircraft**. DroneDeploy's Blog, 2017. Disponível em: <https://blog.dronedeploy.com/choosing-the-right-mapping-drone-for-your-business-part-i-multi-rotor-vs-fixed-wing-aircraft-6ec2d0

DYRMANN, M.; KARSTOFT, H.; MIDTIBY, H. S. Plant species classification using deep convolutional neural network. **Biosystems Engineering**, Elsevier, v. 151, p. 72–80, 2016.

FASTIE, C.; JOGNSON, R.; MCCOLLAM, S. **Correlating Nitrogen Application Rates in Sugarcane With Low-Cost Normalized Difference Vegetation Index (NDVI)**. 2018. Disponível em: <https://projects.sare.org/sare_project/fs14-282/>.

FILHO, J. E. R. V. Expansão da fronteira agrícola no brasil: desafios e perspectivas. Instituto de Pesquisa Econômica Aplicada (Ipea), 2016.

FISCHLER, M. A.; BOLLES, R. C. Random sample consensus: A paradigm for model fitting with applications to image analysis and automated cartography. **Commun. ACM**, ACM, New York, NY, USA, v. 24, n. 6, p. 381–395, jun. 1981. ISSN 0001-0782. Disponível em: <http://doi.acm.org/10.1145/358669.358692>.

FLOYD, R. W. Algorithm 97: Shortest path. **Commun. ACM**, ACM, New York, NY, USA, v. 5, n. 6, p. 345–, jun. 1962. ISSN 0001-0782. Disponível em: <http://doi.acm.org/10.1145/367766.368168>.

GLOBAL, E. **How digital agriculture and big data will help to feed a growing world**. EY, 2017. Disponível em: <https://www.ey.com/en_gl/advisory/how-digital-agriculture-and-big-data-will-help-to-feed-a-growing-world>.

HAN, Y. et al. Automated coregistration of multisensor orthophotos generated from unmanned aerial vehicle platforms. **Journal of Sensors**, Hindawi, v. 2019, 2019.

HARRIS, C.; STEPHENS, M. A combined corner and edge detector. In: **In Proc. of Fourth Alvey Vision Conference**. [S.l.: s.n.], 1988. p. 147–151.

HASSANPOUR, M.; JAVAN, F. D.; AZIZI, A. Band to band registration of multi-spectral aerial imagery–relief displacement and miss-registration error. **International Archives of the Photogrammetry, Remote Sensing & Spatial Information Sciences**, 2019.

HAZAYMEH, K.; HASSAN, Q. K. Spatiotemporal image-fusion model for enhancing the temporal resolution of Landsat-8 surface reflectance images using MODIS images. **Journal of Applied Remote Sensing**, SPIE, v. 9, n. 1, p. 1 – 14, 2015. Disponível em: <https://doi.org/10.1117/1.JRS.9.096095>.

HONG, G.; ZHANG, Y. Wavelet-based image registration technique for high-resolution remote sensing images. **Computers & Geosciences**, v. 34, n. 12, p. 1708 – 1720, 2008. ISSN 0098-3004. Disponível em: <http://www.sciencedirect.com/science/article/pii/S0098300408001544>.

HUNT, E. R. et al. Acquisition of nir-green-blue digital photographs from unmanned aircraft for crop monitoring. **Remote Sensing**, v. 2, p. 290–305, 2010.

HUNTER, M. C. et al. Agriculture in 2050: Recalibrating Targets for Sustainable Intensification. **BioScience**, v. 67, n. 4, p. 386–391, 02 2017. ISSN 0006-3568. Disponível em: <https://doi.org/10.1093/biosci/bix010>.

IHUOMA, S. O.; MADRAMOOTOO, C. A. Recent advances in crop water stress detection. **Computers and Electronics in Agriculture**, Elsevier, v. 141, p. 267–275, 2017.

ISIK, S. A comparative evaluation of well-known feature detectors and descriptors. **International Journal of Applied Mathematics, Electronics and Computers**, v. 3, 01 2014.

JHAN, J.; RAU, J. A normalized surf for multispectral image matching and band co-registration. **International Archives of the Photogrammetry, Remote Sensing & Spatial Information Sciences**, 2019.

Khan, M. J. et al. Modern trends in hyperspectral image analysis: A review. **IEEE Access**, v. 6, p. 14118–14129, 2018. ISSN 2169-3536.

KHANAL, S. **Remote Sensing in Precision Agriculture**. 2017. Disponível em: <https://ohioline.osu.edu/factsheet/fabe-5541>.

KRUSKAL, J. On the shortest spanning subtree of a graph and the traveling salesman problem. In: **Proceedings of the American Mathematical Society**. [S.l.: s.n.], 1956. p. 48–50.

KUMAR, R. M.; SREEKUMAR, K. A survey on image feature descriptors. **Int J Comput Sci Inf Technol**, v. 5, p. 7668–7673, 2014.

LEITE, P. et al. Hidden markov models for crop recognition in remote sensing image sequences. **Pattern Recognition Letters**, v. 32, p. 19–26, 01 2011.

LEUTENEGGER, S.; CHLI, M.; SIEGWART, R. Y. Brisk: Binary robust invariant scalable keypoints. In: **2011 International Conference on Computer Vision**. [S.l.: s.n.], 2011. p. 2548–2555. ISSN 2380-7504.

LIN, C.-Y. et al. Overview of precision agriculture with focus on rice farming. In: **INTERNATIONAL WORKSHOP ON ICTs FOR PRECISION AGRICULTURE**. [S.l.: s.n.], 2019. p. 19.

LOWE, D. G. Distinctive image features from scale-invariant keypoints. **International Journal of Computer Vision**, v. 60, n. 2, p. 91–110, Nov 2004. ISSN 1573-1405. Disponível em: <https://doi.org/10.1023/B:VISI.0000029664.99615.94>.

MA, W. et al. Remote sensing image registration with modified sift and enhanced feature matching. **IEEE Geoscience and Remote Sensing Letters**, v. 14, n. 1, p. 3–7, Jan 2017. ISSN 1545-598X.

MAES, W. H.; STEPPE, K. Perspectives for remote sensing with unmanned aerial vehicles in precision agriculture. **Trends in Plant Science**, v. 24, n. 2, p. 152 – 164, 2019. ISSN 1360-1385. Disponível em: <http://www.sciencedirect.com/science/article/pii/S1360138518302693>.

MAIR, E. et al. Adaptive and generic corner detection based on the accelerated segment test. In: DANIILIDIS, K.; MARAGOS, P.; PARAGIOS, N. (Ed.). **Computer Vision – ECCV 2010**. Berlin, Heidelberg: Springer Berlin Heidelberg, 2010. p. 183–196. ISBN 978-3-642-15552-9.

MATAS, J. et al. Robust wide-baseline stereo from maximally stable extremal regions. **Image and vision computing**, Elsevier, v. 22, n. 10, p. 761–767, 2004.

MATHWORKS. **Align multiple scenes into a single image using image registration**. 2018. https://www.mathworks.com/discovery/image-registration.html [Online; retirado em 15-Dezembro-2018 as 17:47].

MELBOURNE, A.; RIDGWAY, G.; HAWKES, D. J. Image similarity metrics in image registration. In: INTERNATIONAL SOCIETY FOR OPTICS AND PHOTONICS. **Medical Imaging 2010: Image Processing**. [S.l.], 2010. v. 7623, p. 762335.

MESKINE, F.; MILOUD, c. e.-m.; TALEB, N. A rigid image registration based on the nonsubsampled contourlet transform and genetic algorithms. **Sensors**, v. 10, p. 8553–8571, 09 2010.

MILICS, G. Application of uavs in precision agriculture. In: _____. [S.l.: s.n.], 2019. p. 93–97. ISBN 978-3-030-03815-1.

MUJA, M.; LOWE, D. G. Fast approximate nearest neighbors with automatic algorithm configuration. In: **In VISAPP International Conference on Computer Vision Theory and Applications**. [S.l.: s.n.], 2009. p. 331–340.

OCHIENG'MC'OKEYO, P. **AUTOMATED CO-REGISTRATION OF MULTITEMPORAL SERIES OF MULTISPECTRAL UAV IMAGES FOR CROP MONITORING**. Tese (Doutorado) — University of Twente, 2018.

OSE, K.; CORPETTI, T.; DEMAGISTRI, L. 2 - multispectral satellite image processing. In: BAGHDADI, N.; ZRIBI, M. (Ed.). **Optical Remote Sensing of Land Surface**. Elsevier, 2016. p. 57 – 124. ISBN 978-1-78548-102-4. Disponível em: <http://www.sciencedirect.com/science/article/pii/B9781785481024500028>.

PICON, A. et al. Deep convolutional neural networks for mobile capture device-based crop disease classification in the wild. **Computers and Electronics in Agriculture**, Elsevier, v. 161, p. 280–290, 2019.

RAZLIGHI, Q. R.; KEHTARNAVAZ, N.; YOUSEFI, S. Evaluating similarity measures for brain image registration. **Journal of visual communication and image representation**, Elsevier, v. 24, n. 7, p. 977–987, 2013.

ROSTEN, E.; DRUMMOND, T. Machine learning for high-speed corner detection. In: LEONARDIS, A.; BISCHOF, H.; PINZ, A. (Ed.). **Computer Vision – ECCV 2006**. Berlin, Heidelberg: Springer Berlin Heidelberg, 2006. p. 430–443. ISBN 978-3-540-33833-8.

RUBLEE, E. et al. Orb: An efficient alternative to sift or surf. In: IEEE. **2011 International conference on computer vision**. [S.l.], 2011. p. 2564–2571.

SÁNCHEZ, J.; MONZÓN, N.; NUEZ, A. S. D. L. An analysis and implementation of the harris corner detector. **Image Processing On Line**, 2018.

SCHRIJVER, R.; POPPE, K.; DAHEIM, C. Precision agriculture and the future of farming in europe. **Teaduslike ja tehnoloogiliste valikute hindamise üksus.[online] http://www. europarl. europa. eu/RegData/etudes/STUD/2016/581892/EPRS_STU (201 6) 581892_EN. pdf (01.05. 2018)**, 2016.

SHI, J.; TOMASI. Good features to track. In: **1994 Proceedings of IEEE Conference on Computer Vision and Pattern Recognition**. [S.l.: s.n.], 1994. p. 593–600. ISSN 1063-6919.

TARABELLA, A.; TRIVELLI, L.; APICELLA, A. Precision agriculture. In: _____. **Food Products Evolution: Innovation Drivers and Market Trends**. Cham: Springer International Publishing, 2019. p. 79–85. ISBN 978-3-319-23811-1. Disponível em: <https://doi.org/10.1007/978-3-319-23811-1_6>.

TAWFEIK, H. M.; HAMZA, E.; SHAWKY, A. Determination of suitable requirements for geometric correction of remote sensing satellite images when using ground control points. **International Research Journal of Engineering and Technology**, v. 3, p. 54, 2016.

THÉAU, J. Temporal resolution. In: _____. **Encyclopedia of GIS**. Boston, MA: Springer US, 2008. p. 1150–1151. ISBN 978-0-387-35973-1. Disponível em: <https://doi.org/10.1007/978-0-387-35973-1_1376>.

TUYTELAARS, T.; MIKOLAJCZYK, K. et al. Local invariant feature detectors: a survey. **Foundations and trends® in computer graphics and vision**, Now Publishers, Inc., v. 3, n. 3, p. 177–280, 2008.

UCHIDA, S. Image processing and recognition for biological images. In: **Development, growth & differentiation**. [S.l.: s.n.], 2013.

WOLBERG, G. **Digital Image Warping**. 1st. ed. Los Alamitos, CA, USA: IEEE Computer Society Press, 1994. ISBN 0818689447.

YASIR, R. **Data Driven Multispectral Image Registration Framework**. Dissertação (Mestrado) — University of Saskatchewan, 2018.

ZARCO-TEJADA, P. J. et al. New tools and methods in agronomy. In: _____. **Principles of Agronomy for Sustainable Agriculture**. Cham: Springer International Publishing, 2016. p. 503–514. Disponível em: <https://doi.org/10.1007/978-3-319-46116-8_33>.